MASTERARBEIT / MASTER'S THESIS

Titel der Masterarbeit / Title of the Master's Thesis

„Cryogenics for Active Hydrogen Targets and Particle Traps“

verfasst von / submitted by

Victoria Kletzl, BSc

angestrebter akademischer Grad / in partial fulfilment of the requirements for the degree of

Master of Science (MSc)

Wien, 2021 / Vienna, 2021

Studienkennzahl lt. Studienblatt / degree programme code as it appears on the student record sheet:	UA 066 876
Studienrichtung lt. Studienblatt / degree programme as it appears on the student record sheet:	Masterstudium Physik
Betreut von / Supervisor:	Priv.-Doz. Dr. Johann Zmeskal

Abstract

The techniques used for cryogenic systems are fundamental in many scientific fields. State-of-the-art particle physics experiments often heavily rely on cryogenics for their success.

The ASACUSA experiment located at the AD hall at CERN investigates the hyperfine structure of hydrogen as well as antihydrogen via measuring their transition frequency (ν_{HFS}). Since CPT invariance postulates them to be of equal value, a discrepancy would indicate physics beyond the Standard Model. An essential part of this high precision experiment is the cusp. There, antihydrogen and hydrogen are formed and polarised, respectively. Since this structure is to be cooled down to temperatures below 10 Kelvin while surrounded by a magnet, techniques to conduct the cooling power of two cold heads inside the magnet are necessary. Therefore, a new cold bore design has been developed. Some of its most important elements have been tested at Stefan Meyer Institute for Subatomic Physics for their thermal conductivity.

At J-PARC, the E57 experiment is looking at the $2p \to 1s$ transition in kaonic deuterium. The energy of the thus released X-rays gives information on the shift and broadening of the ground state induced by the strong interaction described by the non-perturbative, low-energetic regime of QCD. Due to a substandard number of X-rays during the last measurements in 2018, a new active target cell is being designed. A fundamental aspect of the changed design is the question of possible electronic feed through materials. Two materials have been tested for providing the necessary qualities of keeping the target tight at the 150 Kelvin regime.

A second experiment looking at the $2p \to 1s$ transition energy of kaonic deuterium is SIDDHARTA-2. Here, the X-ray detectors are surrounding the target cell holding the deuterium. However, methods are needed to keep the detectors' temperature at optimal temperature range. Possible methods have been tested.

Zusammenfassung

Die Techniken für kryogenische Systeme sind fundamental für viele wissenschaftliche Felder. Hochmoderne Teilchenphysik-Experimente beruhen oft auf Kryogenik.

Das ASACUSA Experiment in der AD-Halle am Beschleunigerkomplex CERN bestimmt die Hyperfeinstruktur von sowohl Wasserstoff als auch Antiwasserstoff durch Messung ihrer Hyperfeinübergangsfrequenz. Da CPT-Invarianz vorhersagt, dass diese gleiche Werte aufweisen, würde eine Diskrepanz auf Physik jenseits des Standardmodels hinweisen. Ein essentieller Teil dieses Hochpräzisionsexperiments ist die sogenannte Cusp, wo Wasserstoff bzw. Antiwasserstoff geformt und polarisiert werden. Da dieser Teil des Experiments zu Temperaturen unter 10 Kelvin gekühlt werden soll, während sie im Zentrum eines Magneten liegt, müssen Techniken gefunden werden, um die Kühlleistung der beiden außerhalb liegenden Kühlköpfe in das Innere weiterzuleiten. Daher wurde ein neues Kühlsystem entwickelt. Einige der wichtigsten Elemente des Systems wurden am Stefan-Meyer-Institut für Subatomare Physik getestet um deren Wärmeleitung zu bestimmen.

Das am J-PARC gelegene Experiment E57 betrachtet den $2p \rightarrow 1s$ Übergang in kaonischem Deuterium. Die Energie des so frei werdenden Photons enthält Information über die Verschiebung und Verbreiterung des Grundzustandes, welche aufgrund des Einflusses der starken Wechselwirkung entstehen. Dies wird durch die nicht-pertubative, niederenergetische QCD beschrieben. Da während der letzten Messungen im Jahr 2018 eine besonders geringe Zahl an Photonen gemessen wurde, wird eine neue, aktive Targetzelle entwickelt. Ein grundlegender Aspekt des überarbeiteten Designs ist die Frage nach elektronischen Durchführungen. Zwei Materialen wurden danach getestet, ob ihre Eigenschaften die Zelle auch im 150-Kelvin-Bereich dicht halten können.

Ein zweites Experiment, das den $2p \rightarrow 1s$ Übergang in kaonischem Deuterium messen soll, ist SIDDHARTA-2. Hier umgeben die Röntgendetektoren die mit Deuterium gefüllte Targetzelle. Allerdings werden Methoden benötigt, um die Temperatur der Detektoren im optimalen Bereich zu halten. Zwei mögliche Methoden wurden dazu getestet.

Acknowledgements

First of all, I want to thank Hannes for his ever lasting patience, his wisdom he was always happy to share with me, and for introducing me to the wonderful world of experimental particle physics. Without you, I would never have gained the insights into so many elementary aspects of working in the field. Every day in the lab with you was a joy.

I also want to thank Eberhard for providing me with the opportunity to work for the ASACUSA collaboration and as a result play my part in the exploration of the most fundamental physical principles.

My time at the SMI would not have been the same without my colleagues. Doris, Julia, Alina, Vicky and Fiona, I will forever cherish the memories of all the lunches when we could not stop laughing. I would also like to thank Mark, Leo and Gerhard for their support. Amit, you will forever be my favourite CERN roommate.

My thanks also go to Irina. Thank you for making me part of such an interesting project and for always providing guidance.

Constanze, you were with me every step of the way throughout my entire studies. I am glad to have found such a loyal friend.

Marlene, I cannot even beginn to express my gratitude to you. This thesis would have never happened if it weren't for your patience, guidance, and most of all, your friendship.

I am also very thankful to have an amazing support system in my family. The "Händelgassengang" and my extended family always believed in me and my ambitions.

I also want to thank my wonderful partner Martin. Thank you for always being there and making me laugh when I need it the most. I love you.

Last but certainly not least, I need to thank my parents. I would not be the person I am today if it weren't for you. Papa, thank you for showing me the beauty of nature from a young age and telling me that girls have a place in science. Mama, thank you for always believing in me, even when I couldn't. This is for you.

Contents

1 Introduction

The development of techniques making the low temperature regime accessible has introduced a myriad of new possibilities, not only in particle physics but also in numerous other fields. This thesis discusses the use of cryogenic techniques at the Stefan Meyer Institute for Subatomic Physics (SMI) in Vienna for three test setups of world-leading particle physics experiments.

Section 2 gives an introduction to the field of cryogenics. In particular, the two types of cryocoolers used for this master thesis, namely Joule-Thompson and Gifford-McMahon refrigerators, are explained in detail. Their inner working structures including brief discussions of the underlying thermodynamic principles are presented.

The later parts of this thesis introduce three state-of-the-art particle physics experiments spanning a great variety of research. In Section 3 the Atomic Spectroscopy And Collisions Using Slow Antiprotons (ASACUSA) experiment at Conseil Européen pour la Recherche Nucléaire (CERN) is discussed. It is currently undergoing a series of upgrades due to the Long Shutdown (LS) 2. One of the essential improvements performed during this period concerns the temperature of the double cusp magnet. Due to the insufficient number of generated antihydrogen atoms, new techniques to enhance their production are needed. One of the deciding factors might be a significant decrease in temperature, as this would result in a lower velocity of positrons and antiprotons, improving the combination probability. Therefore, a new cold bore had to be developed. The design, testing setup and resulting decisions concerning used materials are a central part of this thesis.

The remaining two experiments presented in Section 4 search for the shift and broadening in the $1s$ state in kaonic deuterium. Although the E-57 experiment at Japan Proton Accelerator Research Complex (J-PARC) and the Silicon Drift Detectors for Hadronic Atom Research by Timing Application (SIDDHARTA)-2 experiment at the Double Annular Φ Factory for Nice Experiments (DAΦNE) are both looking at the same physical process, their execution is quite different. In addition, both use the same detectors for X-ray detection, namely Silicon Drift Detectors (SDDs). This thesis will discuss the tests performed at SMI regarding improvement of the target cells and SDD arrangements for both experiments.

2 Cryogenics

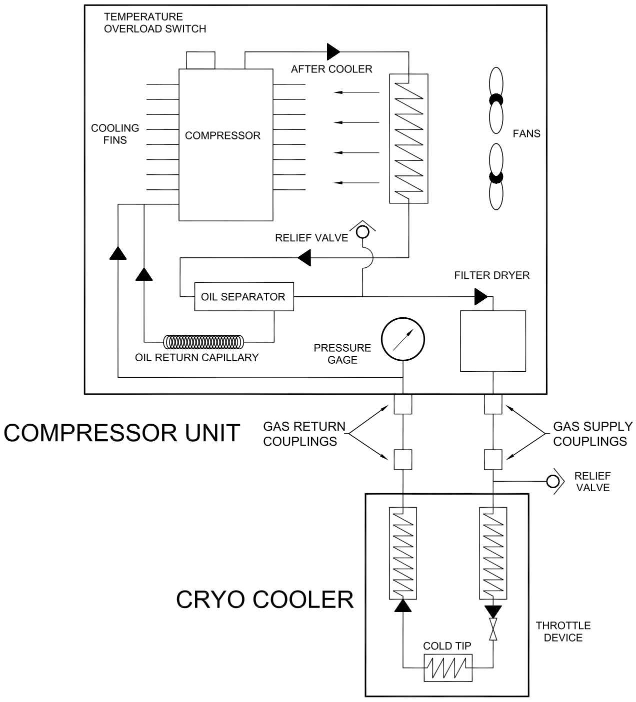

Figure 1: Diagram of a Cryotiger system. *Picture taken from [1].*

Cryogenics are not only the techniques used to reach very low temperatures, but also the methods to measure those temperatures [2]. There are numerous possibilities of cooling systems readily available, such as Stirling refrigerators, pulse tube refrigerators or a variety different kinds of cryostats. For details concerning those cooling systems refer to [3].

This section introduces two standard methods of arriving at cryogenic temperatures which were used during the work performed for this thesis. Both of them are so-called cryocoolers, meaning that they are table-top sized apparatuses which can cool down an experimental system to a certain temperature. The final temperature is determined by the type of cryocooler used. However, the two techniques presented here are very different. The first machine discussed is the Joule-Thompson refrigerator. It operates by a constant influx of high pressure gas at room temperature. The second cooling implements the Gifford-McMahon technique where a pressurised, room temperature gas is used in a cooling cycle consisting of four intermediate steps.

2.1 Cryocoolers

2.1.1 Joule-Thomson Refrigerators

This section describes the working method of the Joule-Thomson refrigeration systems, also known as Linde-Hampson coolers after their inventors Carl von Linde and William Hampson [4]. A drawing representing the standardised Joule-Thomson cryocooler in form of a so-called Cryotiger system is printed in Figure 1. Such a machine consists of a compressor unit, a cryocooler – also called a cold head – and two lines connecting these two parts.

The refrigeration gas is condensed in the compressor unit. Since this is an isothermal process keeping the gas at room temperature, the generated heat has to be given off using cooling fins for air cooling and the after cooler. After having passed through oil and moisture removing components, the gas moves through the high pressure line to the cold head. There it is lead through a heat exchanger where the refrigerant is pre-cooled by the gas leaving the cold head on its way to being re-compressed. Being cooled almost to goal temperature, the now liquid and gas mixture passes an adiabatic flow resistance "which can be a needle valve, a porous plug, a narrow slit, etc." [4], *page 388*. Due to the Joule-Thomson effect, the refrigerant cools down even further when pressure is reduced while the enthalpy is conserved. The liquid refrigerant is gathered in the cold tip where heat exchange with the applied load takes place. The heat from the load is given off to the liquid, resulting in evaporation of some of the refrigeration agent. The outflowing low pressure gas is now returned to the compressor via the heat exchanger where it is pre-cooling the inflowing gas [1, 4].

Depending on the type of refrigerant gas, a temperature of down to 70 K can be reached using Joule-Thomson refrigeration in a Cryotiger system. If lower temperatures are desired, helium is a possible refrigerant, making the 4 Kelvin range accessible. However, due to its low inversion temperature, helium needs to be pre-cooled, as the gas temperature increases when expanded at constant enthalphy at room temperature. As a result, a different method is needed when wanting to work with helium using a single system, namely Gifford-McMahon refrigeration.

2.1.2 Gifford-McMahon Refrigerators

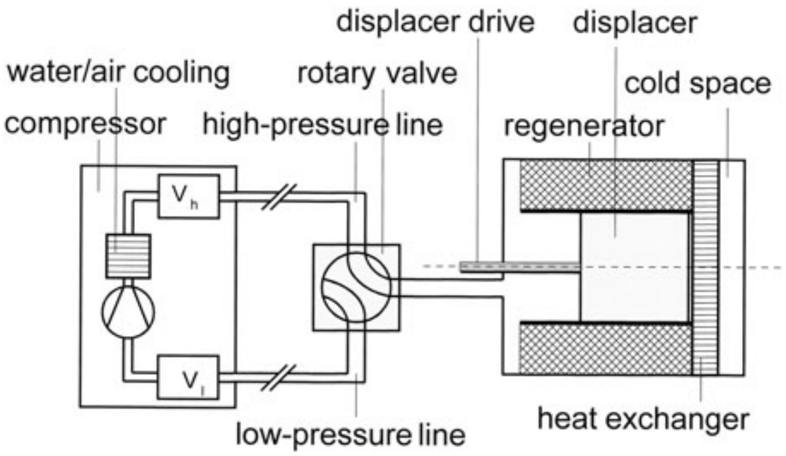

Figure 2: Diagramm of a Gifford-McMahon cryocooler. *Picture taken from* [3].

This section discusses the working mechanisms of Gifford-McMahon (G-M) cryocoolers, which are in use in a wide variety of applications [2, 3]. A schematic drawing of the working principle of this type of machine is shown in Figure 2. This cryocooler uses helium as a working fluid, making the 4 Kelvin temperature range accessible. The cold head is again connected to the low and high pressure side of a compressor via two lines and rotating valves. The displacer and regenerator are located inside the cold head and usually encompassed in one structure.

The material used for the regenerator is an essential part of the proper cryocooler design. It is made up of solid but porous material with high heat capacity and good thermal contact to the gas, while having low flow resistance. These are contradictory demands which make regenerator development extremely demanding [3].

As a first step, the helium gas is compressed in an isothermal process. The heat generated during compression is discharged using air and, more importantly, water cooling. The compressed gas then flows through the high pressure line to the cold head. There, a four step cycle takes place in order to cool down the refrigerant [2, 3]:

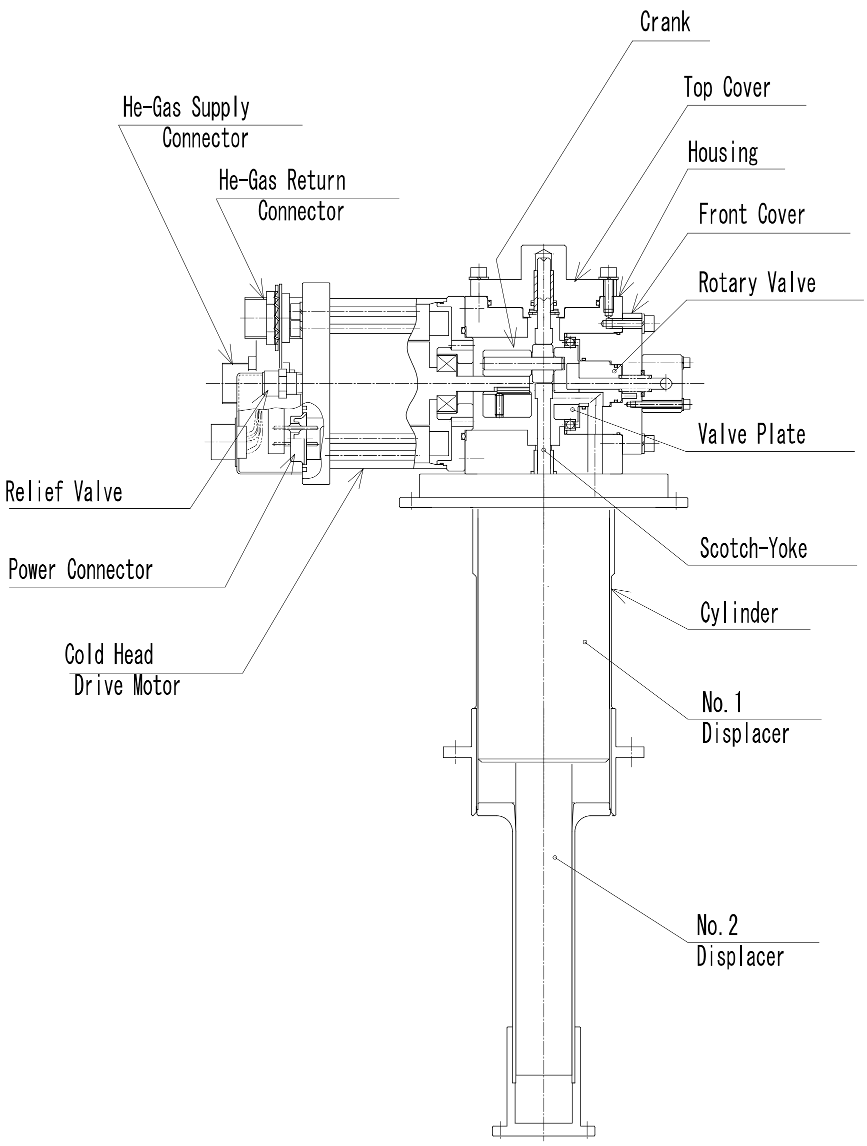

Figure 3: Diagramm of a two step G-M refrigeration system. *Picture taken from* [5].

1. The displacer is located at the right hand side of the cylinder shown in Figure 2. The cold head is connected to the high pressure line leading from the compressor to the rotary valve. The gas enters the cylinder.

2. The displacer moves to the left of the cylinder. The gas passes through the regenerating material towards the cold end. If this is not the first cycle, the helium is being pre-cooled meaning heat from the gas is absorbed by the regenerator.

3. The rotary valve connects the cold head to the low pressure line, while the displacer stays in place on the left end of the cylinder. Therefore, some of the gas passes the regenerator and the gas in the cold end expands, resulting in a cooling effect.

4. The displacer moves towards the cold end, pushing out all of the remaining gas. During this process, the cooled gas passes through the regenerator, taking up some of its heat and therefore cooling the material. As a result, the inflowing gas of the next cycle will be pre-cooled to lower temperatures than the gas in the previous one.

Modern G-M refrigerators are offered in two varieties: single or two step systems. The single step method has been discussed thus far. A diagram of a two step system is displayed

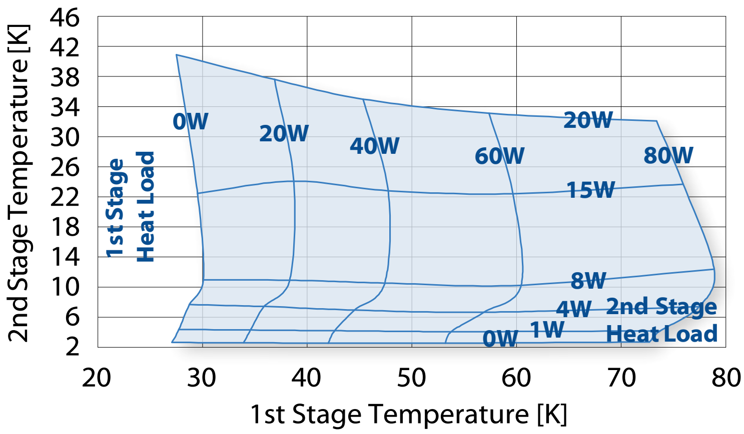

Figure 4: Capacity map for the SRDK-408D2 cold head using a 50 Hz compressor and 6 m helium gas lines. *Picture taken from* [6].

in Figure 3. This method has two displacers intricately working together in order to achieve temperatures as low as 4 K. As a result, the two steps reach different temperatures, the lower temperature occurring on the second step. In order to determine the lowest possible temperature accessible by amount of heat load, one can refer to capacity maps such as the one shown in Figure 4. The x-axis gives the temperature on the first step and the y-axis the second step's temperature. The light blue lines determine how much heat load one can attach to the first and the second stage respectively when aiming for specific temperatures.

3 The ASACUSA Experiment

This section discusses the ASACUSA experiment at CERN. First, an introduction to the physics behind the search for CPT invariance in general, and the experiment in particular are given. Then, the experiment's setup will be discussed. The new and old cold bore are presented in detail. Finally, the tests performed at SMI and the resulting decisions for the final cold bore will be presented.

3.1 Introduction

3.1.1 Antimatter and CPT violation

The Standard Model (SM) is one of the most successful theories in the history of physics. It anticipated numerous particles which have only been found in the decades since the theory's development. One of the most important predictions was that of antiparticles being the result of the negative energy solutions of the Dirac equation [7]. Shortly after, in 1932, the positron was discovered in cosmic rays using a vertical Wilson chamber [8]. The discovery of the antiproton followed in 1955 at the Bevatron proton beam [9]. The SM predicts antiparticles and particles to share all properties apart from the sign of their charge and their inner quantum number which are exactly opposite.

The SM demands the equal production of matter and antimatter. If matter and antimatter had been produced with the same quantity during the Big Bang, all of it should have been consumed by annihilation processes briefly after. However, since the existing universe is made of matter, it can be concluded that it must have surpassed antimatter by a minuscule quantity. One of the possible effects causing this so-called baryon asymmetry is the violation of the CPT theorem. This states that any physical law must be conserved under combined Charge (C) conjugation and Parity (P) operation and Time (T) reversal. An investigation of possible Standard Model Extension (SME) is presented by D. Colladay and V. A. Kostelecky in [10] which adds CPT and Lorentz violating terms while regarding the SM as the low-energy limit.

An overview on existing experiments exploring CPT invariance is given in Figure 5. Since the hydrogen atom is one of the best studied systems in physics, it has been proposed as a promising testing ground of the CPT theorem [11].

3.1.2 The ASACUSA Collaboration

The ASACUSA experiment is performed by an international collaboration located at the Antiproton Decelerator (AD) facility at CERN. The collaboration has a variety of scientific goals:

- The measurement of the hydrogen as well as the antihydrogen hyperfine structure using a Rabi-type spectroscopy method in search of CPT violation [12].
- Measurements of antiproton-nuclei annihilation cross sections at low energies through antiproton-nuclei collisions [13]. In addition, fragmentation studies in the annihilations have recently been added to the agenda [14].
- Performing laser-spectroscopy on antiprotonic helium. This measurement could also be an indicator for CPT violation by precise measurement of the antiproton mass [15].

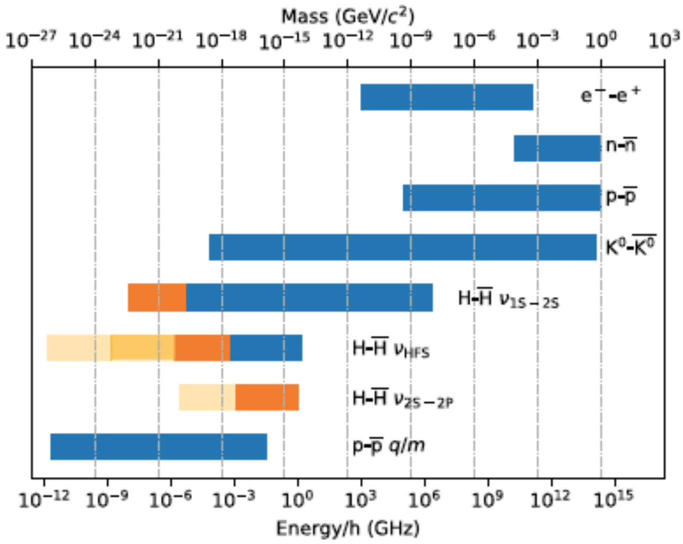

Figure 5: Overview of existing experiments exploring CPT violation. The blue bars represent existing experiments with the type of system being studied noted to the right. The length of the bars represents the relative precision, the absolute precision is given by the left end of the bars. The right ends indicate the measured quantity. Orange bars represent the achievable precision if state-of-the-art sensitivity for hydrogen is reached. For the hyperfine transition frequencies ν_{HFS} the orange colour represents the initial goal of ASACUSA collaboration, paler orange gives the expected precision for line width for a fountain and yellow represents results using a hydrogen maser. For the $2s \rightarrow 2p$ transition (Lamb shift) the orange bar indicates the estimated precision, the yellow gives the accuracy for hydrogen. *Picture taken from* [12].

3.1.3 Measurement of the ν_{HFS}-Transition

The measurement of the ground state hyperfine transition frequency (ν_{HFS}) of hydrogen (H) as well as antihydrogen ($\bar{H}$) by the ASACUSA collaboration is based on the experiment proposed by Rabi et. al. [16] for measuring the nuclear magnetic moment. A schematic drawing of this method as conducted by Rabi and his colleagues is shown in Figure 6. This section gives a brief introduction, more detailed descriptions can be found in e.g. [17].

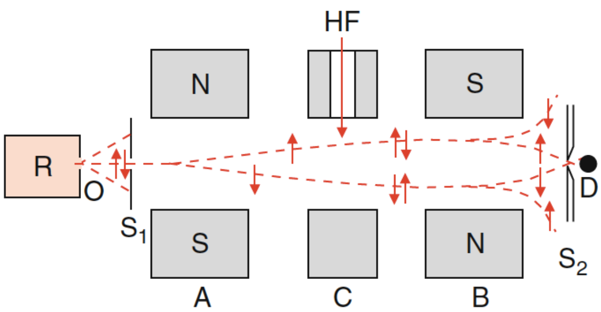

Figure 6: Schematic drawing of the Rabi method. A beam of atoms is given off by a source R, passes through the first aperture S_1, three magnets A,C, and B. After the second aperture S_2 the atoms are counted by a detector D. *Picture taken from* [18].

Atoms are ejected from a source R and transverse an aperture S_1 resulting in a narrow beam. Then they pass through an inhomogeneous magnetic field produced by magnet A where the atoms experience a force $\vec{F} = \vec{m}\nabla\vec{B}$ with $\vec{m}$ being the magnetic moment of the atom and $\vec{B}$ the external magnetic field. Due to this force, the atoms are diverted from their original path according to their respective magnetic moments. The magnet B produces an inhomogeneous

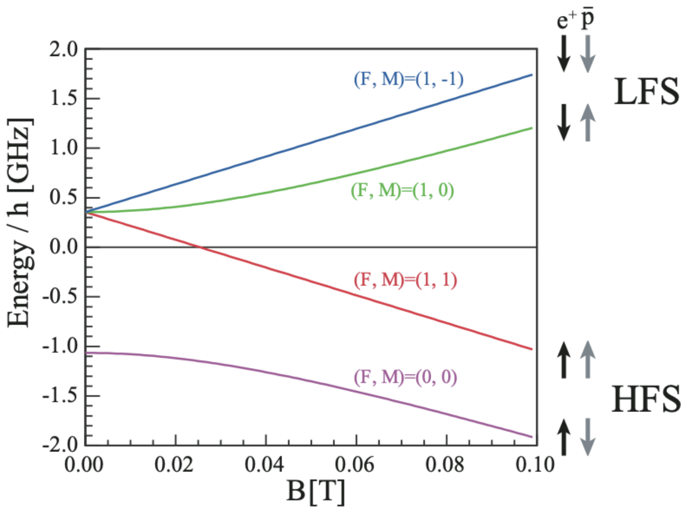

Figure 7: Splitting of the hyperfine energy levels of hydrogen and antihydrogen ground states. Two states on top are low field seekers, lower two are high field seekers. *Picture taken from* [19].

magnetic field with inverse field gradient to the field of magnet A. As a result, the atoms are diverted into the opposite direction, redirecting them towards the detector D located behind the second aperture S_2. In order to have the atoms transition between quantised states of the magnetic moment, two structures are inserted between magnets A and B. Firstly, a third magnet C introduces a homogeneous field leading to a splitting of the energy levels. Secondly, a high frequency source HF is introduced, producing an oscillating field perpendicular to the magnetic field of magnet C. If the frequency of the oscillating field is in accordance with a dipole transition between two neighbouring Zeemann-states, the magnetic moment $\vec{m}$ of the atom is changed by the transition between states. Since $\vec{m}$ has now been altered, the atom passing through the inhomogeneous field produced by B is diverted away from detector D. As a result, the transition frequency can be determined by counting the atoms arriving at D. A scan shows a drop in beam intensity at the transition frequency.

Depending on the positron's and antiproton's spin orientations, four energy levels are possible in the $\bar{H}$ ground state [19]. These are shown in Figure 7. The splitting of the hyperfine energy levels results in two groups of states:

- The upper two states in Figure 7 represent low field seeking states. If the external magnetic field $\vec{B}$ increases, the energies of these two states increase correspondingly. Therefore, they are attracted to lower field regions.

- The lower two states in Figure 7 are high field seeking states. Their energy decreases with increasing $\vec{B}$ field, attracting them to higher field regions.

Depending on the applied magnetic field, one of the two types of states can now be focused on a detector. Introducing the right oscillation frequency can defocus the beam due to a switch between the states, indicating the hyperfine transition frequency.

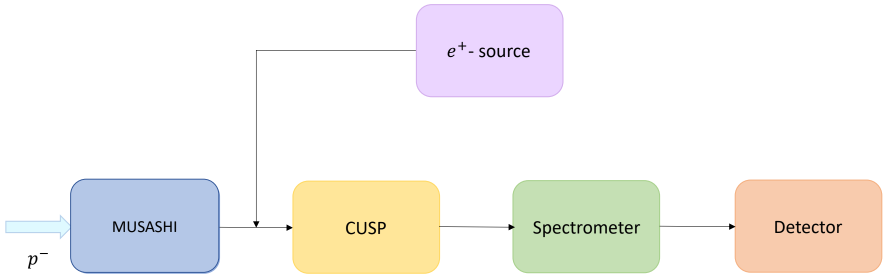

Figure 8: Schematic drawing showing the ASACUSA setup at the AD hall

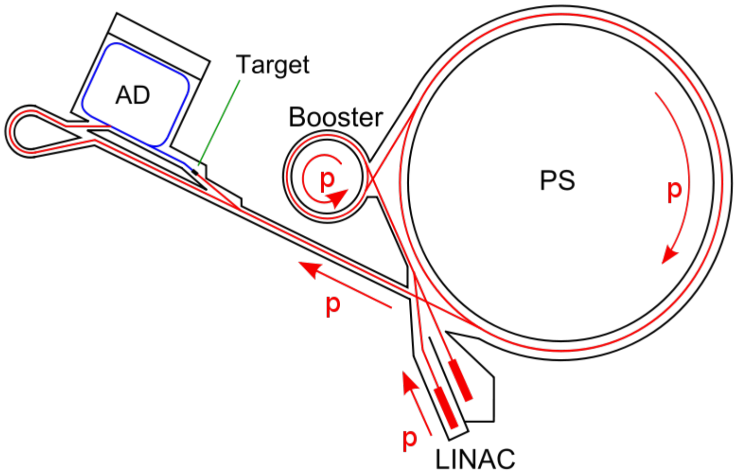

Figure 9: The CERN acceleration complex delivering to the AD. The red lines and arrows give the location and orientation of the proton beam, the antiproton beam is shown in blue. *Picture taken from* [20].

3.1.4 Setup at CERN

This section gives a brief introduction to the experimental setup at the AD. A schematic overview of the ASACUSA setup is shown in Figure 8.

In order to produce antihydrogen, two different kinds of antiparticles need to be available and, subsequently, combined: antiprotons ($\bar{p}$) and positrons (e^+). The latter are much more easily accessible. The ASACUSA collaboration uses a ^{22}Na source, emitting positrons via β^+ decay, resulting in a maximum kinetic energy of 545 keV [21]. The extracted positrons are then cooled down via a solid neon moderator and gathered using a buffer gas trap [22].

The production of antiprotons, and slow $\bar{p}$ in particular, is significantly more advanced. For ASACUSA they are supplied by CERN's accelerator complex. An overview is displayed in Figure 9. In the first step of the process towards slow $\bar{p}$, hydrogen atoms are stripped of their shell and accelerated to an energy of 50 MeV by the LINear ACcelerator (LINAC) 2. In the next two steps, the protons are injected into the Proton Synchrotron Booster (PSB) and the Proton Synchrotron (PS), resulting in an acceleration to 1.4 GeV and 25 GeV, respectively. At this point, some of the protons are directed towards experimental facilities such as the AD, while the rest is injected into the Super-Proton Synchrotron (SPS) and, finally, into the Large Hadron Collider (LHC) [23]. In order to produce antiprotons, the 25 GeV proton beam coming

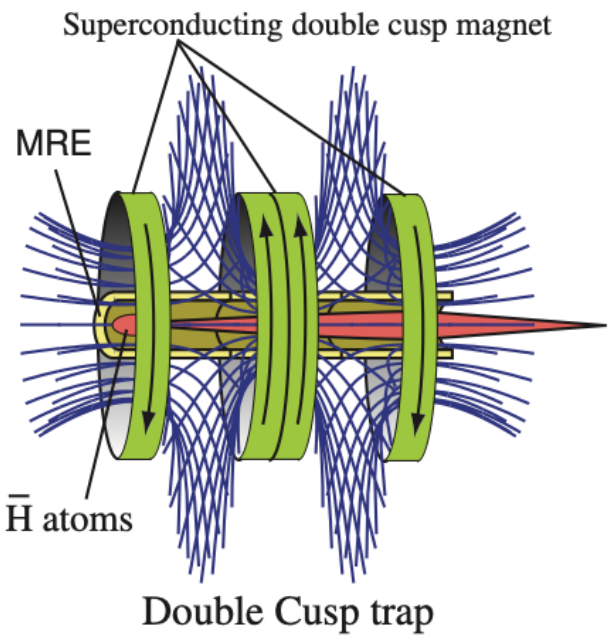

Figure 10: Schematic diagram of the ASACUSA cusp magnet. The green elements represent the Helmholtz coils with the current orientation given by black arrows. The blue lines represent the field lines produced by the coils. The red element shows the form of the $\bar{H}$ beam which is enclosed by MREs. *Picture taken from* [19].

from the PS is directed onto a target where the following process takes place:

$$p\,(\text{beam}) + p\,(\text{target}) = p + p + p + \bar{p}$$

The extracted $\bar{p}$ have a mean energy of 3.6 GeV. In order to form antihydrogen and its subsequent use for spectroscopy, the antiprotons' energy needs to be decreased by eight orders of magnitude. The AD synchrotron reduces the energy to 5.3 MeV via numerous techniques [24]. After the ongoing Extra Low Energy Antiproton (ELENA) upgrade until summer of 2021, the antiprotons will enter the experimental area with a kinetic energy of around 100 keV.

After this deceleration process, the $\bar{p}$ enter a Multi-Ring Trap (MRT), also called the Monoenergetic Ultra-Slow Antiproton Source for High-precision Investigation (MUSASHI) [25]. There, around 1.2×10^6 antiprotons can be captured, stored and cooled to energies of 10-100 eV using a non-neutral plasma of electrons.

In the next step, antiprotons and positrons from the ^{22}Na source are jointly injected into the double-cusp [19], where they combine to form antihydrogen. It also acts as a polariser for the produced $\bar{H}$ atoms. A sketch of the cusp's magnetic configuration is shown in Figure 10. A cross-sectional view of the cusp including its cooling structures is shown in Figure 11 in the next section. Two pairs of anti-parallel Helmholtz-coils form the superconducting double-cusp magnet. A set of Multi-Ring Electrodes (MREs) is located at the centre of the coils. The mixing of $\bar{p}$ and e^+ takes place in the upstream region of the cusp, the two areas where $\vec{B} = 0$ show a high focusing performance for low field seeking states.

Another important part of the cusp is the ASACUSA Micromegas Tracker (AMT) located between the MRE and the cold bore. The detector is made of two connected half cylinders of Micro-MEsh Gaseous Structure (Micromegas). Each of the cylinders consists of two layers of Micromegas which are separated by one cylindrical layer of scintillators used for triggering. The AMT detects annihilation processes and their location within the cusp.

A Rabi type spin flip cavity (as described above) is used as a spectrometer [26]. At the current state of the experiment, this part has been removed since the main goal is to increase the number of produced $\bar{H}$ [14]. Furthermore, the spin flip cavity is currently undergoing improvement at an additional setup using an atomic hydrogen beam [27].

The final apparatus of the ASACUSA setup is the antihydrogen detector [14]. It consists of two elements. Firstly, a scintillator of Bismuth Germanate (BGO) acts as a calorimeter. Secondly, a hodoscope detector surrounding the calorimeter is used for tracking the products of antiproton-matter annihilations. The latter is again divided into two sub-detectors: (1) two layers of scintillating plastic bars (for x- and y-resolution) and (2) two layers of scintillating fibres (for resolution in z-direction).

3.2 The Previous ASACUSA Cold Bore

In order to minimise the number of annihilations of antiprotons and antihydrogen with residual gas in the cusp, a pressure in the rage of 10^{-12} mbar must be reached. This is possible if the cusp is cooled down to less than 6 K [25, 28]. This section discusses the design of the ASACUSA cold bore as used until the LS 2 of CERN. It is shown in Figure 11. This section is based on the work of M. Shibata et. al. and gives a brief overview, for details and exact dimensions refer to [28].

The cryogenic system is being cooled by two G-M-type cryocoolers of the model Iwatani HE15 with cooling powers of 1.5 W at 4.2 K and 15 W at 30 K, respectively. They are positioned at either side of the cusp magnet. Their second stages attach to the Inner Vacuum Chamber (IVC) via pairs of copper strips. These are made of 6N (99.9999%) ultra high purity copper with excellent thermal conductivity. In addition, the strips were annealed for 1 hour at 800 °C. The IVC is made of a 316 l stainless steel tube and contains the MRE stack. Surrounding it, there are two half cylinders of 6N copper foil with a thickness of 2.5 mm. The copper strips are connecting the cold head to the IVC. A sheet of copper called the "copper collar" is wrapped around the IVC. One bellow is attached on either end of the IVC tube. Due to their low thermal conductivity, they provide the necessary temperature gradient to connect the 4 K stage to the room temperature parts of the remaining experimental setup.

A radiation shield of Oxygen Free Copper (OFC) and aluminium is mounted around the 4 K region and the cold heads. They are thermally connected to the first stage of the G-M cryocoolers. The radiation shield is surrounded by a layer of superinsulation in order to keep the heat load of the Outer Vacuum Chamber (OVC) onto the radiation shield as low as possible. The OVC is kept at room temperature [28].

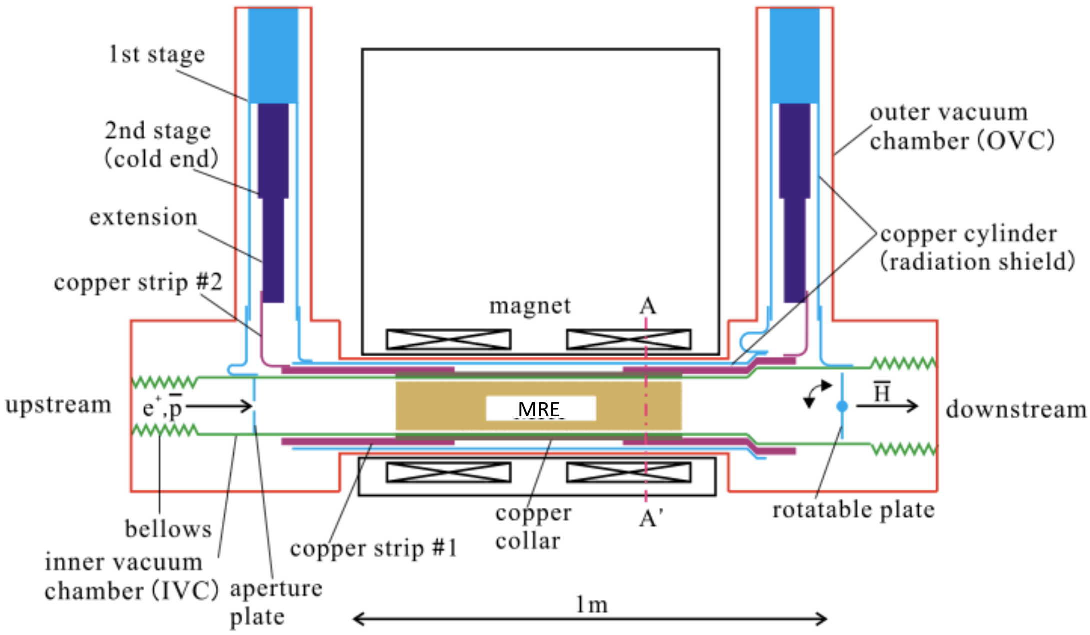

(a) Cross-section of the ASACUSA cusp. The e^+ and $\bar{p}$ enter to the left and the formed $\bar{H}$ atoms exit the structure to the right.

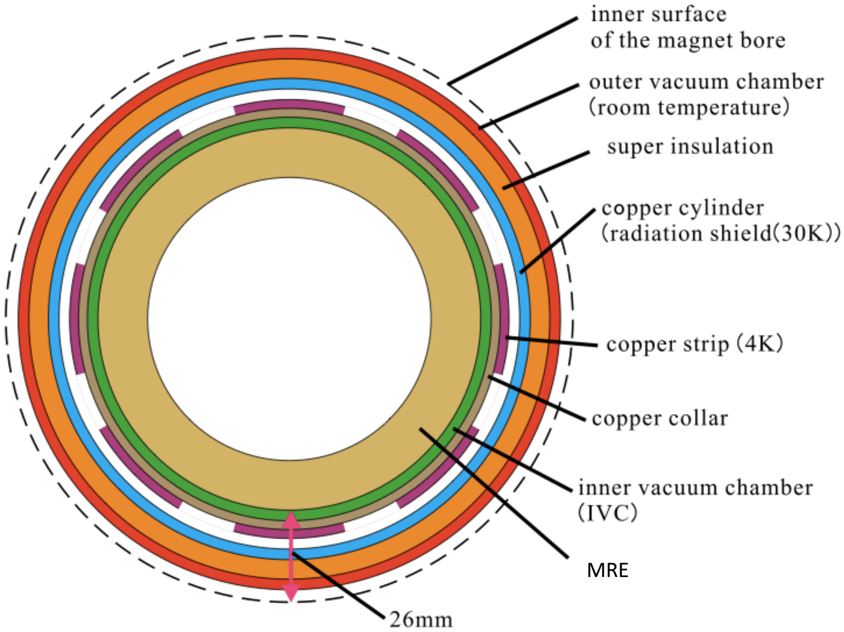

(b) Cross-section of setup's cryogenic structure. View is perpendicular to (a) along dashed line between A and A'.

Figure 11: Cross-sectional views of the ASACUSA cusp including the old cold bore design. *Pictures adapted from* [28].

3.3 The New Cold Bore Design

Two drawings of the new cold bore design are presented in Figure 12. The main structure using two cold heads to cool the cusp from either side is kept the same. The used cold heads are however upgraded to the RDK-408D4 model manufactured by Sumitomo Heavy Industries with a cooling power of 2 W at 4 K each [29]. Both their first and second stages are used for cooling parts of the setup.

The first stage is expected to reach a temperature of about 30 to 40 K. Therefore, the heat shield shown in green in Figure 12 (a) is from now on referred to as the 40 K shield since it is cooled down via connections to the cryocoolers' first stage. It is made up of two types of aluminium (Al). The shield surrounding the MREs is made of 5N (99.999%) pure aluminium. The other parts of the shield are made of standard Al. The connection between first stage and shield is achieved by using a bundle of 5N aluminium wires with a diameter of 1 mm each. They are held together by a surrounding coat of indium welded onto the wires by high pressure. On the lower stream side, this kind of connection is also used to connect the second stage to the parts kept at 4 K. It is essential, that these connections between the 4 Kelvin stage and the cold bore structure are flexible. This is due to the fact, that the MRE stack has to be movable in order to manually align it with the external magnetic field.

On the upstream side (the left hand side in Figure 12 (a)) the sample holder of the cold head attaches to a Oxygen-Free High thermal Conductivity (OFHC) copper block. It is connected to a second copper block via several strips of 5N aluminium. This second copper block is the mounting structure for the cold bore elements leading along the MREs. For cooling, four 5N aluminium rods are used due to their excellent thermal conductivity at cryogenic temperatures [30]. These rods are shown in Figure 12 in blue. In addition, four ordinary aluminium rods are mounted onto the copper flange for structural support of the MREs as shown in Figure 12 (b). The cooling of the MRE stack is achieved by high purity copper plates which connect them to the 5N aluminium rods. In order to ensure thermal but no electric conductivity between rods at ground and the electrodes laying at high voltage, the copper plates are electrically insulated using 50 μm kapton foil.

Due to the fact that the cusp is the only cryogenic part of the ASACUSA experiment, there is an almost 300 K temperature difference between the cold bore and the attaching stream line. As a result, a component with a big enough temperature gradient is needed. Bellows satisfy this demand. They are made up of several individual membranes which are welded together. This results in a low thermal conductivity. In order to ensure a minimisation of heat load on the 4 K stage, systems of two bellows are mounted on either end of the cusp as shown in Figure 12. The outer bellows connect to room temperature on one side and to the first stage of the cold heads (40 K stage) on the other. The inner bellows also connect to the first stage on one end and to the 4 K stage on the other. This construction should provide a satisfactory temperature gradient.

As already mentioned, the cold bore and the MREs structure must be movable to guarantee that manual alignment is possible. Since opening the cusp is very time consuming, it is essential that this can be achieved from the outside. As a result, either end of the bore will be hung up by nylon cables. These will be accessible from the outside for adjustment.

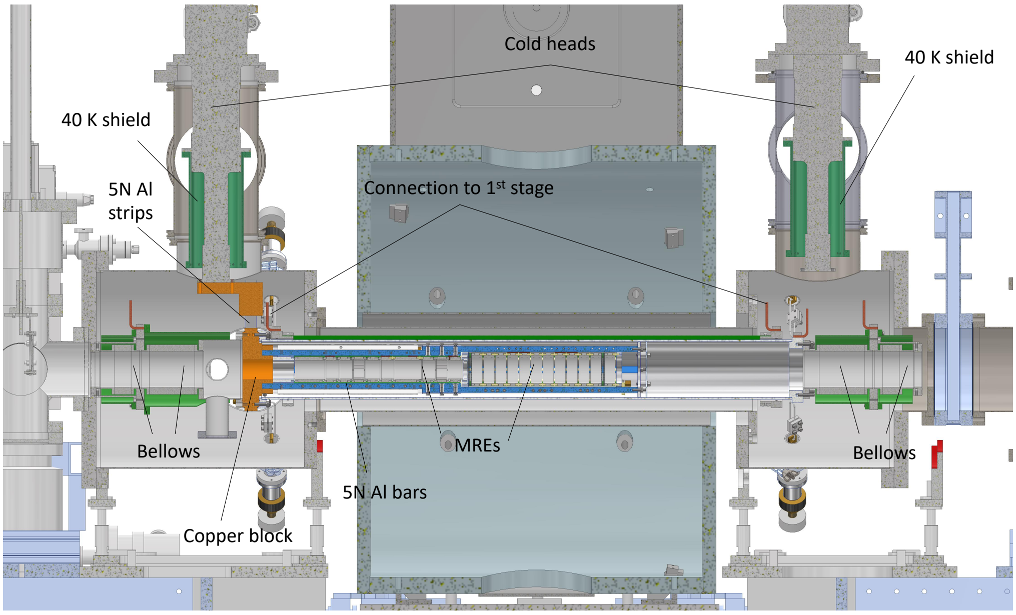

(a) Drawing of the new cold bore design showing both cold heads, the 40 K shield (green), the two copper blocks (orange) and the 5N aluminium bars (blue)

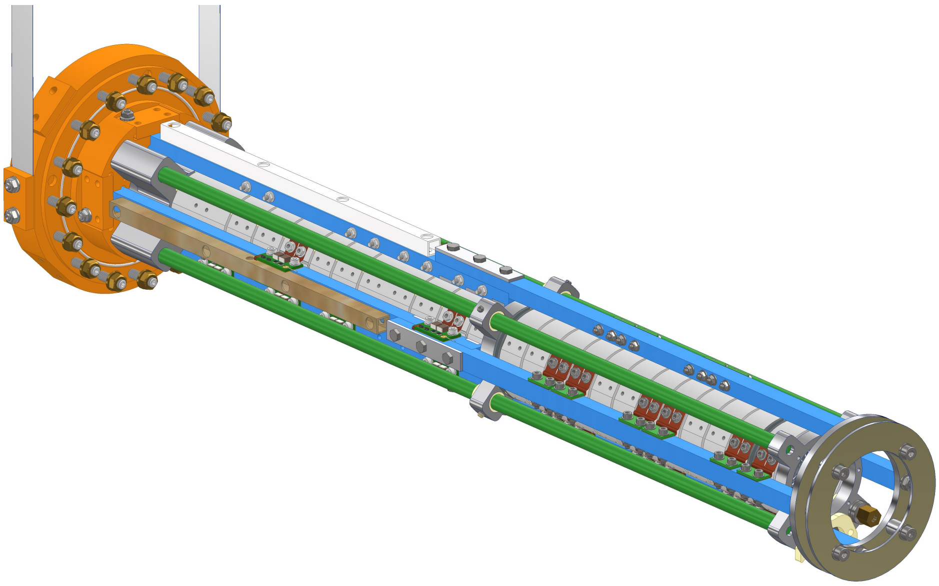

(b) The new cold bore structure surrounding the MREs.

Figure 12: Drawings of the new ASACUSA cold bore design. *Courtesy of D. Pristauz-Telsnigg, SMI.*

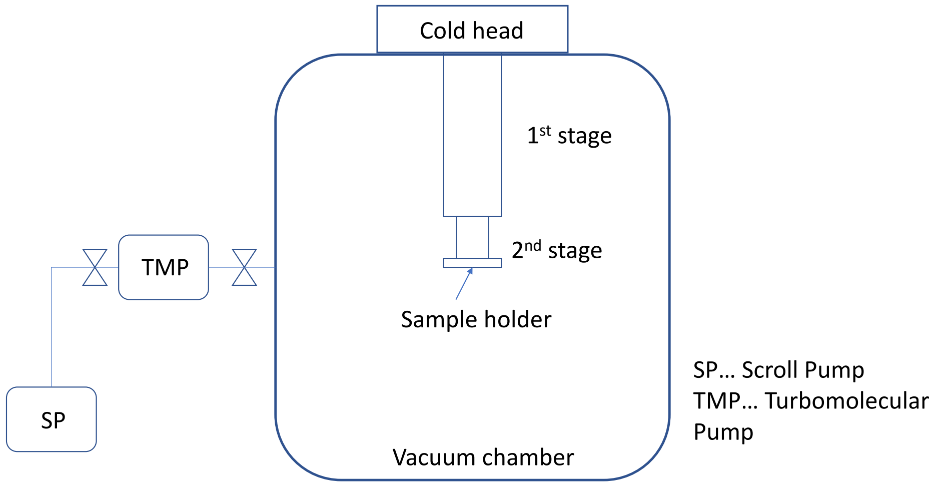

Figure 13: Layout of the ASACUSA setup at SMI.

3.4 Setup at SMI

A schematic drawing of the basic ASACUSA testing setup used for this thesis is shown in Figure 13.

For reaching a desired vacuum pressure in the lower 10^{-6} mbar range at room temperature, a two step pumping system is used. An Edwards aXDS15i scroll pump and a TurboMolecular Pump (TMP) of the type Turbo.Power 300 manufactured by Leybold are used. They are separated from the main vacuum chamber by a gate valve.

The cryocooler used is a G-M type SHI-APD Cryogenics RDK-408D2 cold head. It is attached to a Sumitomo CSW-71 compressor which is water cooled. The resulting cooling power is given by the manual to be 1 W at 4.2 K [5].

Not shown in Figure 13 are several feed through options connecting the used heating resistors and temperature sensors to outside the vacuum. The temperature sensors used are four DT-670 silicon diodes (numbered Diodes 1-4). These are read out by a Lake Shore ultra-low cryogenic temperature controller Model 350. For read out, the chart recording software of the manufacturer is used. The resistors are of the type RTO 50 F 22 R with a $\pm 5\%$ tolerance and are operated via a GW Instek GPS-4303 power supply.

These basic components of the testing setup remain unchanged during all consecutive measurements. Therefore, the following sections present the various components attached to the sample holder of the cold head.

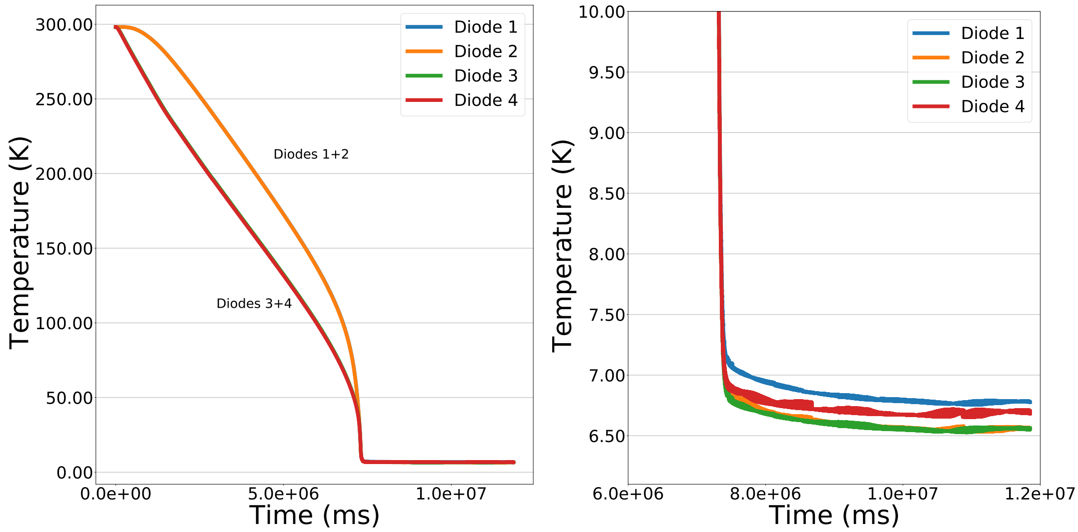

(a) Cooling process of aluminium rod setup.

(b) Final temperatures of testing setup.

Figure 14: Temperature measurement during cooling process of the two 5N Al rod setup.

3.5 Testing the 5N Aluminium Rods

A central part of the new cold bore design presented in Section 3.3 are the four 5N aluminium rods. These are responsible for removing the heat from the MREs. As a result, they need to display excellent thermal conductivity. This section discusses the setup, measurements and results of the tests done with two exemplary 5N aluminium rods.

3.5.1 Setup

Pictures taken from the testing setup of the 5N aluminium rods are shown in Figure 15.

The mounting structure of the rods consists of two aluminium flanges, each of which holds one DT-670 diode (Diodes 3 and 4). Opposite of the temperature sensor on the flange located closer to the sample holder (visible on the right of Figure 15 (c)), a RTO 50 F 22 R heating resistor is attached (Resistor 3).

The 5N aluminium rods are held by clasps on the second flange. The rods are 50 cm long with a diameter of 1 cm. They are mounted on one side to the second aluminium flange by a clasping mechanism. On the other end of each of the rods, a small clasp is located. On both clasps one temperature sensor (Diodes 1 and 2) and one RTO 50 F 22 heating resistor (Resistors 1 and 2) are mounted.

Before moving the structure into the vacuum chamber, several layers of superinsulation are wrapped around the different components in order to prevent heat radiation from warming the setup. Good heat transfer is achieved by adding a mixture of vacuum grease and silver powder between all contact areas of different components, e.g. between the cold head's sample holder and the first aluminium flange. Therefore, a temperature of about 6.6 K can be reached as shown in Figure 14.

(a) Mounting of the 5N aluminium bars. They are attached to the sample holder of the cold head via two aluminium flanges (bottom).

(b) Aluminium clasp mounted to the ends of the rods. Each holds one temperature sensor (left) and one heating resistor (right).

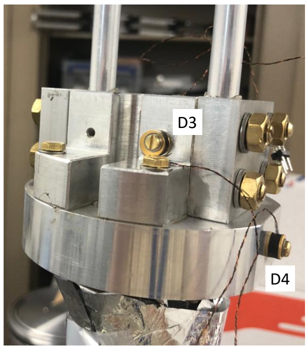

(c) Two aluminium flanges attaching the rods to the sample holder of the cold head. Both hold one temperature sensor.

Figure 15: Mounting of 5N aluminium rods, temperature sensors and heat resistors.

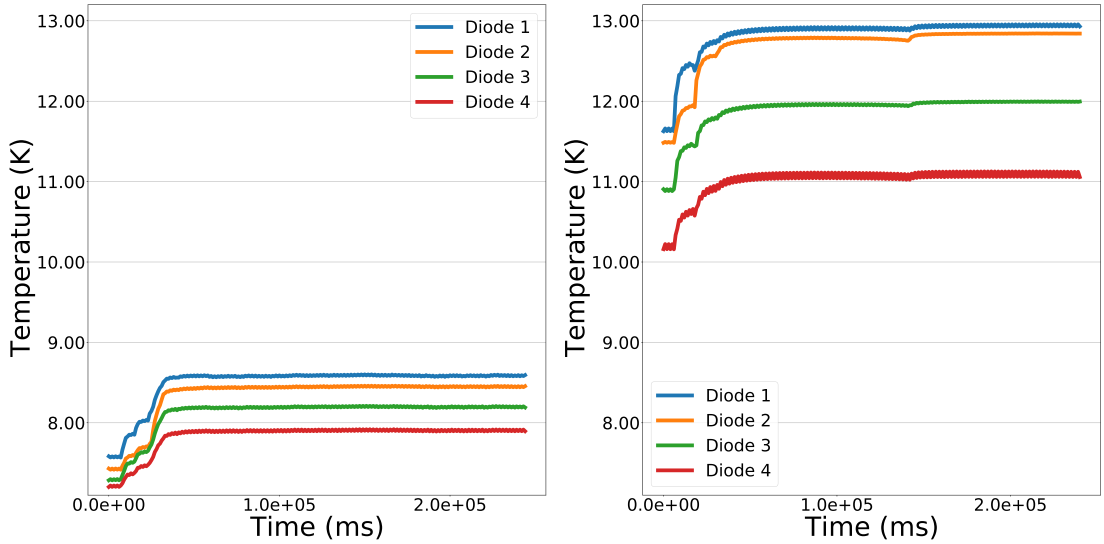

(a) Measurement with 0.5 W input on Resistors 1 and 2.

(b) Measurement with 2 W input on Resistors 1 and 2.

Figure 16: Temperature curves for first measurements performed only using Resistors 1 and 2.

3.5.2 Measurements

In order to determine the thermal conductivity of the aluminium rods, two sets of measurements are performed.

Firstly, the setup is only heated via Resistors 1 and 2. The temperature increase is recorded for all four diodes using the Lake Shore temperature controller. The following heating input is supplied to the system for each resistor: 0.25 W, 0.5 W, 1.0 W, 1.5 W and 2.0 W. The measurements for each heating value were performed over a duration of three to five minutes until equilibrium was reached along all parts of the setup. Examples of the resulting temperature curves are shown in Figure 16 for 0.5 W and 2 W.

Secondly, Resistor 3 is used to keep the temperature for Diode 3, and therefore on the second aluminium adapter flange, constant at 10 K. This was achieved by using the setpoint-function on the Lake Shore temperature controller. After a period of 10 minutes equilibrium is reached. Due to the temperature constraint of 10 K, measurements are performed with 0.5 W and 1 W only. These powers are again supplied by Resistors 1 and 2. The measured temperature curves are shown in Figure 19. The stabilised temperature of Diode 3 of 10 K is clearly visible.

Both types of measurements are repeated once in order to check for their reproducibility.

In order to extract the thermal conductivity of the aluminium rods, the data is analysed using Excel. The temperature is determined by calculating the mean value of the data within the last 100 s (100 data points) of the measurement. The uncertainty is then calculated using Excel's STDEV.P function. The thus determined temperature values and their respective uncertainties are given in Tables 18 - 20 in Appendix A.

3.5.3 Results

The thermal conductivity of the 5N aluminium rods is calculated using the following equation:

$$\lambda = \frac{q \cdot L}{A \cdot \Delta T} \tag{3.1}$$

where

- q is the power input.
- L is the length between the points of temperature measurement, i.e. distance between Diodes 1 and 3 as well as Diodes 2 and 3. It is supposed to be (50 ± 1) cm.
- A presents the cross section area of the rods. Since the radius is 0.5 cm, the area is calculated to be (0.785 ± 0.032) cm^2.
- ΔT represents the temperature difference between two points of measurement, i.e. the ends of the rods and the aluminium flange.

Measurements using Resistors 1 and 2

The thermal conductivity is calculated using equation 3.1 above. The results are displayed in Tables 1 and 2 for the first and second measurement respectively. The combined data is also presented in Figure 17.

When regarding Figure 17, it is obvious that the data is split into two separate lines for λ_{13} and λ_{23}. This is most probably due to the effect of the different temperatures extracted from the sensors. When regarding Figure 16, the temperature of Diode 1 clearly lies above the one measured by Diode 2 in both cases. Therefore, ΔT between Diodes 1 and 3 is bigger than ΔT between Diodes 2 and 3. Taking into account that it is a factor in the denominator of equation 3.1, the smaller ΔT results in a higher λ_{23}. The temperature difference between the two sensors might be the result of two independent effects. Firstly, the values measured by the diodes might depend on their manufacturing. This is indicated by the fact, that the final temperatures after cooling are $T = (6.782 \pm 0.003)$ K for Diode 1 and $T = (6.565 \pm 0.003)$ K for Diode 2. However, the temperature difference between Diodes 1 and 2 decreases with increasing power input so that the discrepancy between the calculated conductivities also decreases. This indicates a difference in thermal conductivity. Since the rods can be assumed to be identical, there probably is a deviation in conductivity due to a slight difference in the clamping, e.g. too little conducting mixture. The results presented in Figure 17 show very good agreement between the two measurements for either Diode pair indicating their reproducibility.

The thermal conductivity of the 5N aluminium rods is given to be in the range of 20 to 200 Wcm^{-1}K^{-1} for the given temperatures [30] as shown in Figure 18. Most importantly, the Figure clearly shows an increase in thermal conductivity in the 1 to 10 K range and a decrease with higher temperatures. This behaviour is also visible for the collected data displayed in Figure 17. Therefore, the results obtained in these measurements are in accordance with the values and behaviour of the thermal conductivity of 5N aluminium given in the literature. This result is especially pleasing considering the fact that the measurement was not simply performed along the rod but included transitions between elements (rods to flange, clasp to temperature sensor, etc.).

Power	λ_{13} (Wcm^{-1}K^{-1})	λ_{23} (Wcm^{-1}K^{-1})
0.25	(51.3 ± 6.6)	(109 ± 17)
0.50	(87.1 ± 7.9)	(134 ± 14)
1.00	(109.0 ± 7.9)	(151 ± 12)
1.50	(125.8 ± 8.1)	(163 ± 12)
2.00	(135.2 ± 8.9)	(152 ± 10)

Table 1: Results for the thermal conductivity of the 5N aluminium rods using the first data set. λ_{13} represents the thermal conductivity between Diodes 1 and 3, λ_{23} the thermal conductivity between Diodes 2 and 3. The given error is calculated using propagation of uncertainty.

Power	λ_{13} (Wcm^{-1}K^{-1})	λ_{23} (Wcm^{-1}K^{-1})
0.25	(47.6 ± 6.2)	(116 ± 18)
0.50	(80.3 ± 7.4)	(132 ± 13)
1.00	(102.3 ± 7.5)	(143 ± 11)
1.50	(120.2 ± 8.0)	(149 ± 11)
2.00	(129.5 ± 8.2)	(151 ± 11)

Table 2: Results of the thermal conductivity for the second measurements. λ_{13} represents the thermal conductivity between Diodes 1 and 3, λ_{23} the thermal conductivity between Diodes 2 and 3. The given error is calculated using propagation of uncertainty.

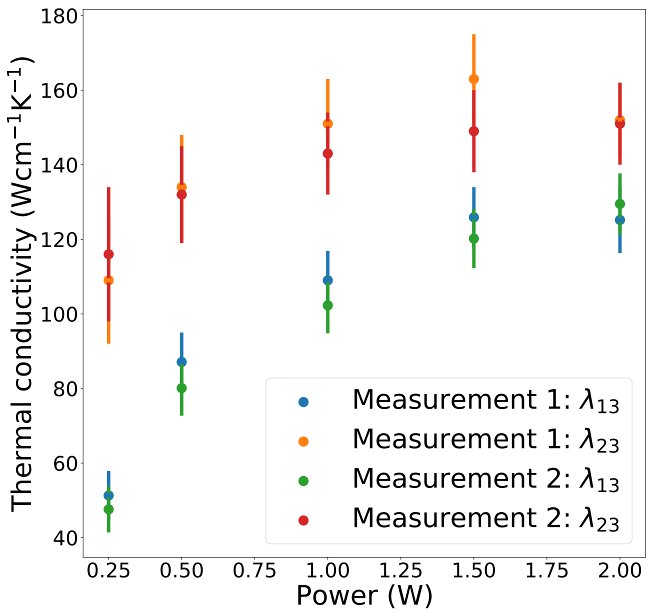

Figure 17: Comparison of the thermal conductivity coefficient determined by the two data sets taken without stabilisation of Diode 3.

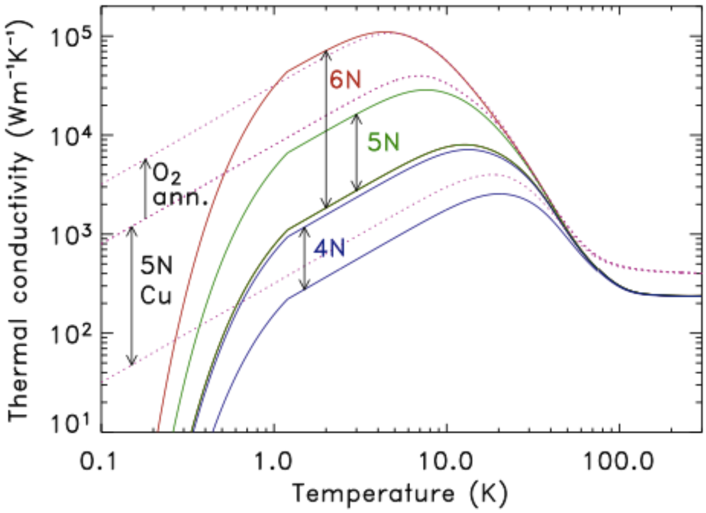

Figure 18: Thermal conductivity of aluminium of different purity in comparison with copper. *Picture taken from* [30].

Power	λ_{13} (Wcm^{-1}K^{-1})	λ_{23} (Wcm^{-1}K^{-1})
0.50	(93.7 ± 9.0)	(83.5 ± 7.9)
1.00	(110.9 ± 7.8)	(134.3 ± 9.5)
0.50	(90.1 ± 8.1)	(83.7 ± 7.5)
1.00	(114.2 ± 8.8)	(140 ± 12)

Table 3: Results for the thermal conductivity of the 5N aluminium rods for the stabilised measurement. Diode 3 was kept at a temperature of 10 K via Resistor 3. The rods were heated via Resistors 1 and 2. The upper two rows give the results from the first measurement. The bottom two rows present the values determined by the second measurement.

Stabilised Measurements

The results obtained for the thermal conductivity of the two 5N aluminium rods for the stabilised measurement are shown in Table 3 and Figure 20. In both cases the data of first and second measurements were combined. The results are, again, in good accordance with the value given in the literature.

However, Figure 19 (a) and (b) show an interesting aspect of the measurements. In contrast to all other data recordings, Diode 2 shows a higher value than Diode 1 in (a). In (b), the recorded temperature for Diode 1 lies again above the value measured by Diode 2. This is due to the fact that the heating resistor stabilising Diode 3 to 10 K has been mounted closer to Diode 2. Therefore, with lower input power by the Resistors 1 and 2, Resistor 3 delivers more power to the structure to ensure the stabilisation of Diode 3 to 10 K. Due to the proximity to Diode 2, this results in a higher temperature for this sensor. When the power input is increased for Diode 1 and 2, the heating by Resistor 2 is decreased, and the effect of deviating temperatures for Diodes 1 and 2 as a result of their manufacturing, as described above, dominates.

To conclude, the measurements show that the thermal conductivity of the 5N aluminium rods is in agreement with the literature is as expected. Therefore, their employment in the new cold bore setup is supposed to successfully deliver the cooling power of the cold head to the entire length of the MREs.

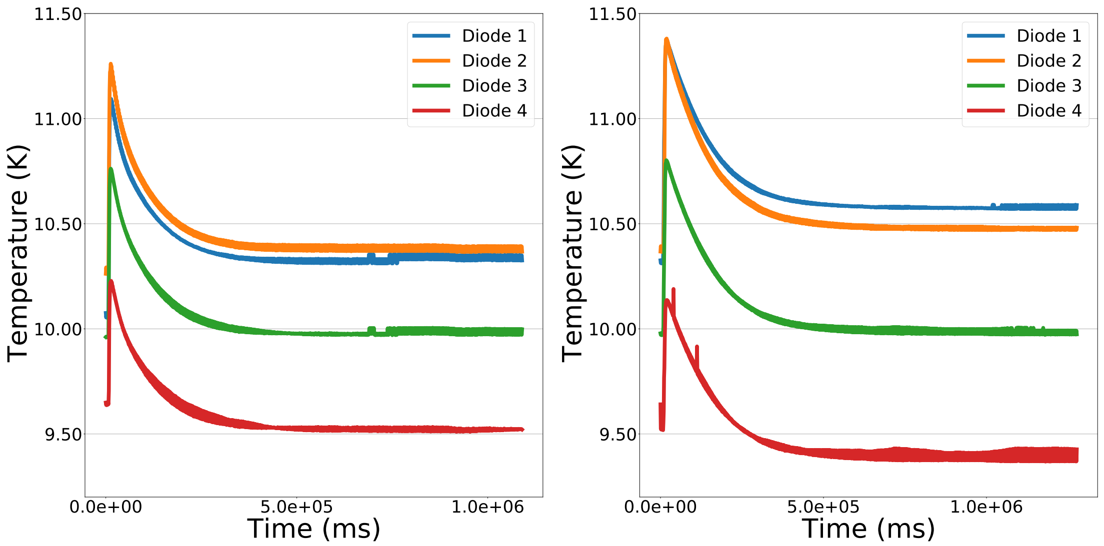

(a) Measurement with 0.5 W input on Resistors 1 and 2 and stabilised temperature of Diode 3.

(b) Measurement with 1 W input on Resistors 1 and 2 and stabilised temperature of Diode 3.

Figure 19: Curves for the first measurement using a Lake Shore temperature controller for keeping Diode 3 at 10 K.

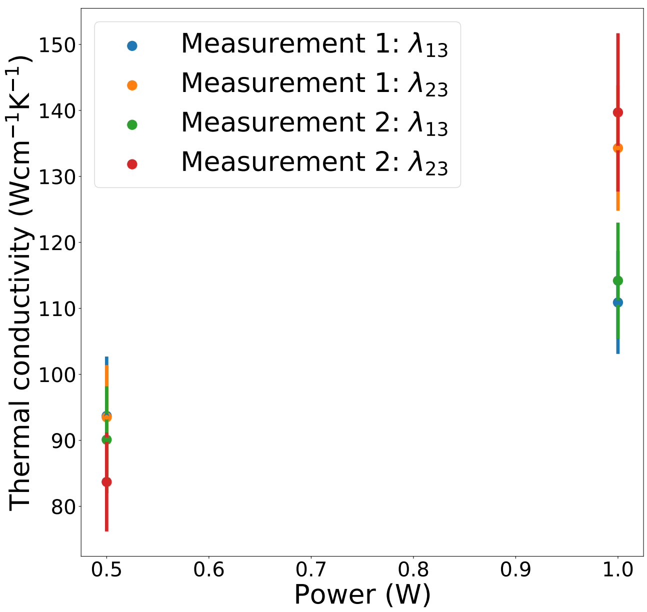

Figure 20: Comparison of the thermal conductivity coefficient determined by the two data sets using the stabilised method.

3.6 Performance of a Single Bellow

In order to separate the 4 K cusp setup from the rest of the experiment, which is kept at room temperature, a component displaying the necessary temperature gradient is needed. Thus, a system of bellows as described in Section 3.3 is chosen. This section describes the test performed at SMI to determine the performance of single such a structure.

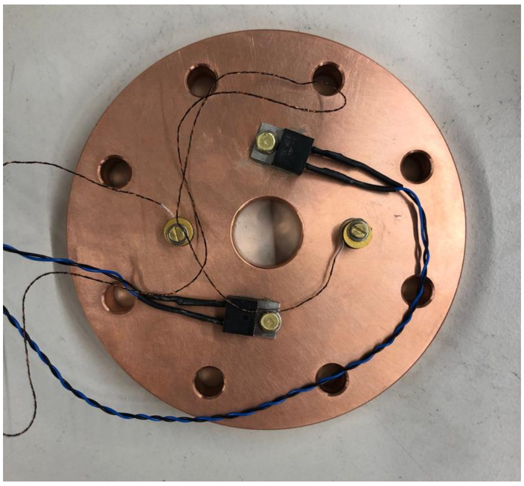

(a) Bottom copper flange with Diodes 1 and 2 and Resistors 1 and 2.

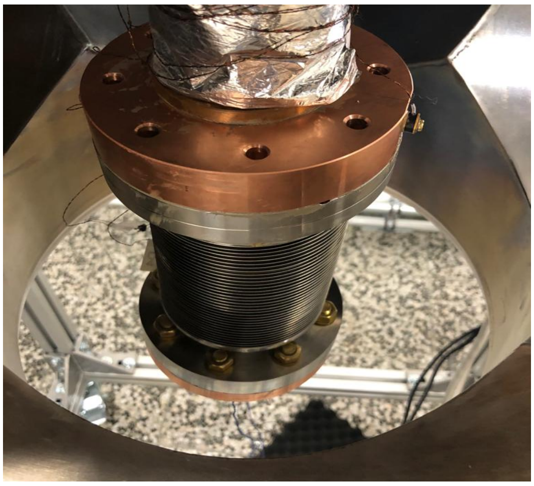

(b) Bellow mounted on cold head in vacuum chamber. Flange shown in (a) is located at the bottom of the hanging structure. Diodes 3 and 4 are mounted to the upper flange attached to the sample holder.

Figure 21: Setup for the bellow tests.

3.6.1 Setup

Pictures taken of the bellow testing setup are shown in Figure 21. The used bellow is a DN 63CF membrane bellow manufactured by PROPHYSIK with the following specifications [31]:

- number of membrane pairs: 34
- inner membrane diameter: 65 mm
- outer membrane diameter: 90 mm
- free length: 152 mm

- compressed length: 88.7 mm
- expanded length: 180.5 mm

In order to attach the bellow to the cold head's sample holder and mount four temperature sensors to the setup, two OFHC copper flanges which are annealed for 24 hours at 250 °C are used. The first, or bottom, flange is shown in Figure 21 (a). It has a diameter of 11.2 cm and a thickness of 2 cm. It holds two temperature sensors (Diodes 1 and 2) and two heating resistors (Resistors 1 and 2). These are identical to the elements used in Section 3.5. The opening in the centre of the flange is necessary for pumping the inside of the bellow.

On the other side, the bellow is mounted to a second flange of same diameter but different thickness (1.2 cm). This upper flange attaches to the sample holder of the cold head. It also holds two more temperature sensors (Diodes 3 and 4). These are located at the sides of the flange as visible in Figure 21 (b).

In order to minimise the influence of heat radiation on the measurement, the testing structure is wrapped in several layers of super insulation. Good heat transfer is again achieved by applying a mixture of vacuum grease with silver powder to all contact areas.

3.6.2 Measurements and Results

Firstly, the bellow's performance during cooling is measured. Figure 22 shows the temperatures registered by the four diodes during the cooling process. The measurement represents a time period of 18 hours or 65000 data points, the maximum possible to save using the Lake Shore software. It is clearly visible that the end of the bellow attached to the cold head is quickly cooled down to a temperature of around 5 K. However, the other side of the bellow is cooled much more slowly. Indeed, the temperature reached by this end after 18 hours of cooling is about 276 K, so not even quite 20 K lower than room temperature. This is a first indicator of the very low thermal conductivity of the bellow structure.

Secondly, the performance of the bellow under the influence of a heat load is tested. Therefore, measurements are performed with 1.0 W and 2.0 W. These are shown in Figures 23 and 24, respectively. The heating power is supplied through heating Resistors 1 and 2. Each has a power output of 0.5 W or 1.0 W, respectively. The measurement performed with an overall input power of 1.0 W is again taken over 18 hours. When supplying the system with 2.0 W, however, the temperature on the warm side of the bellow heated up significantly faster, as visible in Figure 24. Therefore, this measurement was stopped after several hours in order to minimise damage on the system due to overheating.

Unfortunately, in neither of the cases equilibrium between the low and high temperature sides could be reached. Still, there are some conclusions to be drawn from the presented data. First of all, as already mentioned, the thermal conductivity can supposed to be extremely small due to the very limited decrease in temperature during the cooling process. Second of all, the influence of high temperatures on the bottom flange has hardly any influence on the cold end. This is best portrayed by the measurement with 1.0 W input shown in Figure 23. Although there is a visible increase in temperature, it only amounts to about 0.25 K on the cold end while the temperature on the heated side rose by over 60 K.

Thus, it can be concluded that the bellows work as expected. They are a very valuable tool to shield the 4 K environment from the connecting elements kept at room temperature. In order to guarantee this successful separation, not one but two bellows will be installed in the final cold bore.

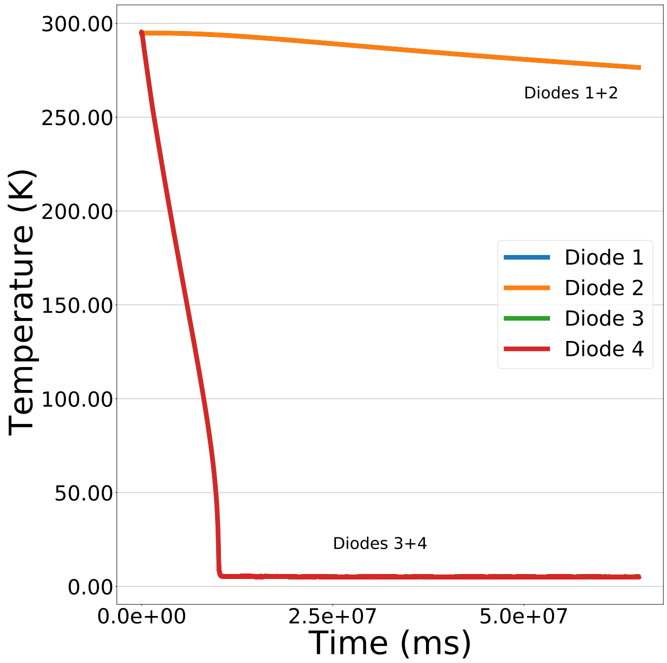

(a) Measured temperatures of all four diodes.

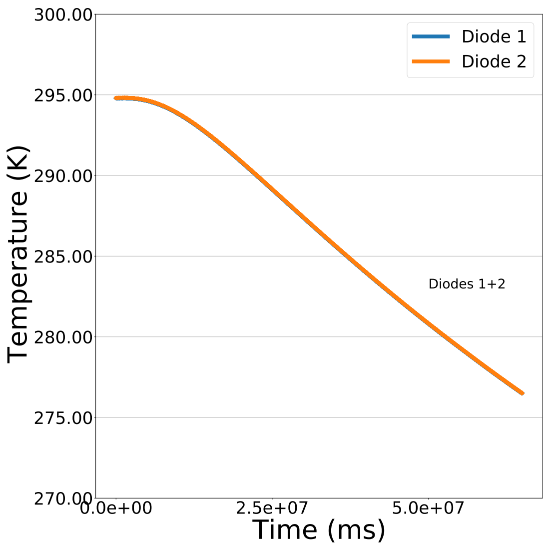

(b) Temperatures reached for the bottom flange with Diodes 1 and 2.

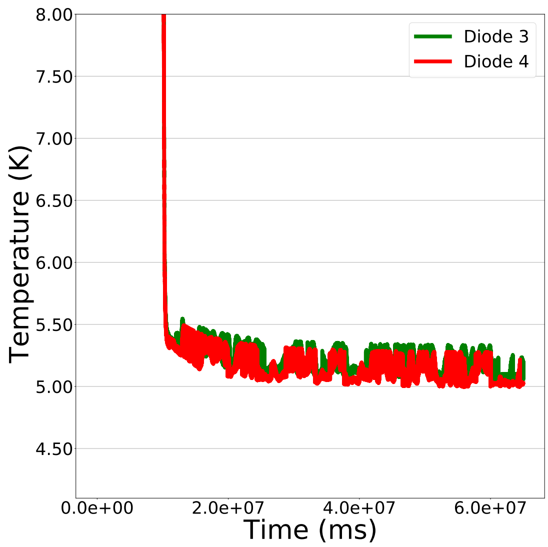

(c) Temperatures reached for the upper flange with Diodes 3 and 4.

Figure 22: Cooling process of the bellow setup. The data was taken over a period of 18 hours.

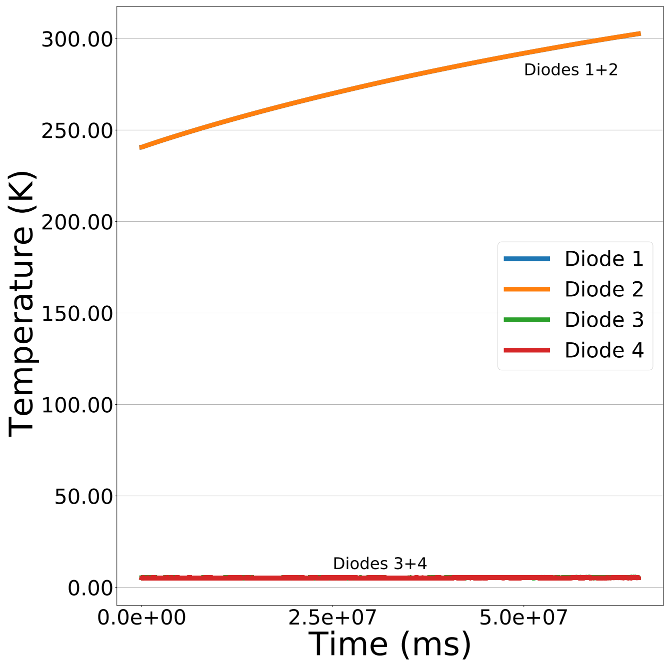

(a) Measured temperatures of all four diodes.

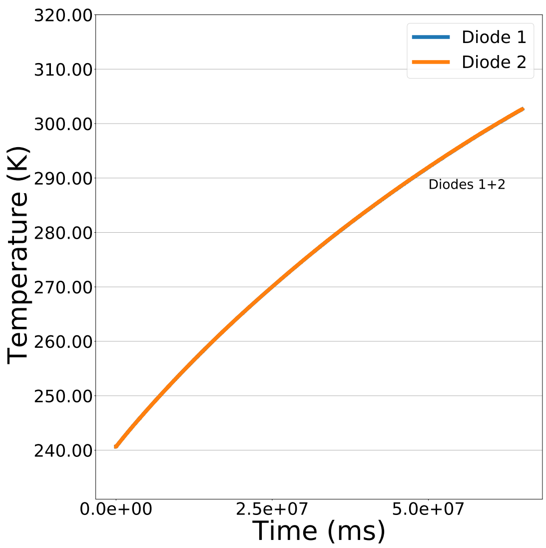

(b) Temperatures reached for the bottom flange with Diodes 1 and 2.

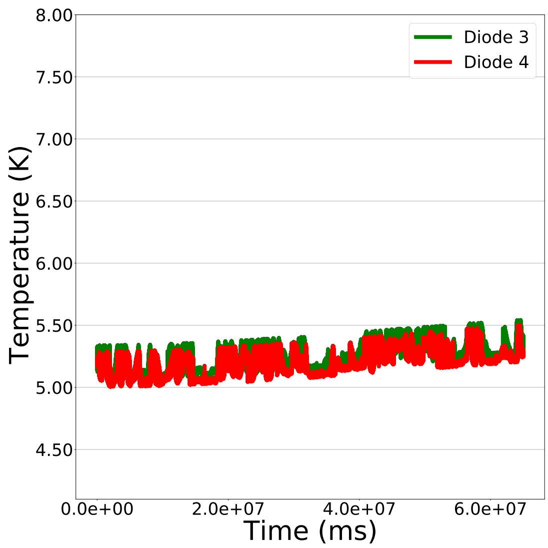

(c) Temperatures reached for the upper flange with Diodes 3 and 4.

Figure 23: Temperatures measured while heating the structure with 1 W of power input. The data was taken over a period of 17 hours.

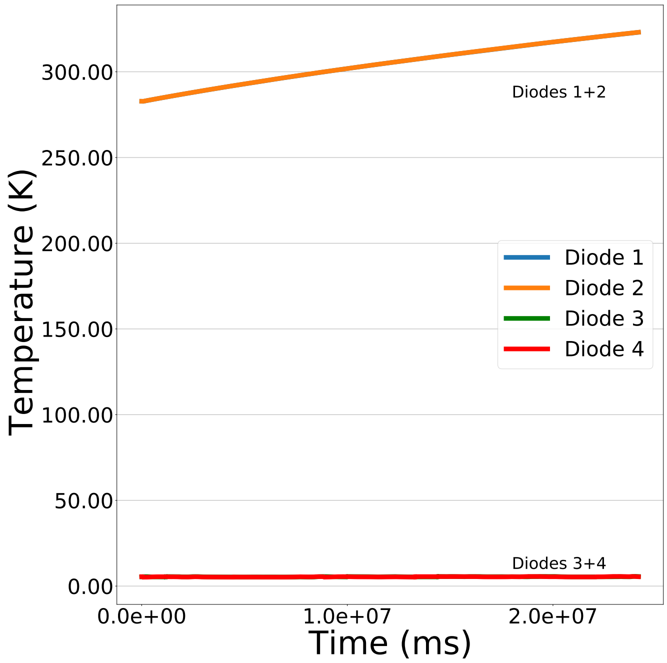

(a) Measured temperatures of all four diodes.

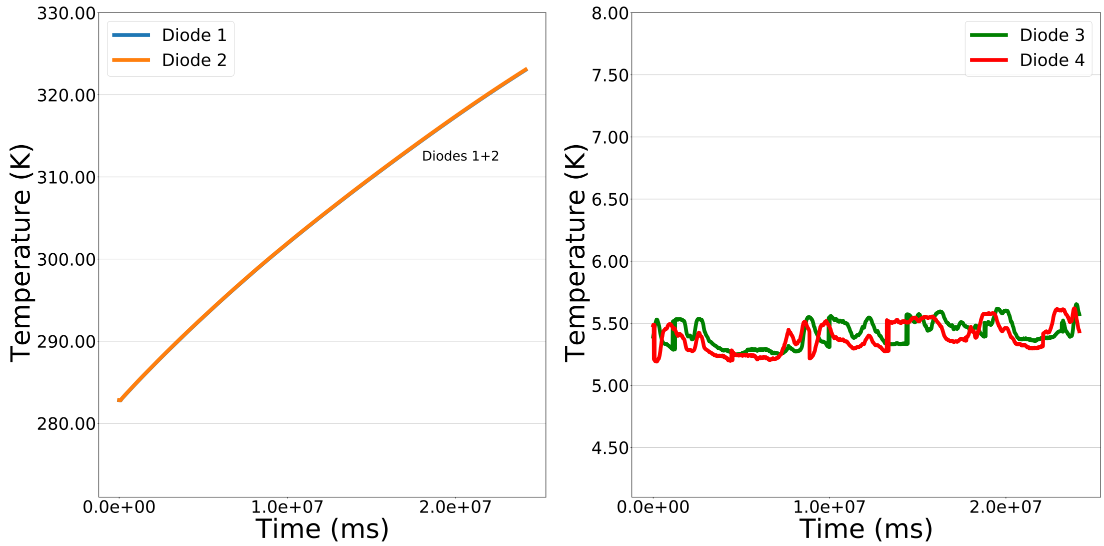

(b) Temperatures reached for the bottom flange with Diodes 1 and 2.

(c) Temperatures reached for the upper flange with Diodes 3 and 4.

Figure 24: Temperatures measured during heating of the bellow testing setup with 2 W. The data was taken over a period of 7 hours.

3.7 Testing the 5N Aluminium Strips

As presented in Section 3.3 the 4 Kelvin stage of the cold head needs to be attached to the cold bore via flexible connections. This poses certain constraints on possible materials since their thermal conductivity needs to be high enough to transmit the cooling power to the bore while still remaining bendable. Therefore, 5N aluminium was again chosen. Thin foil of high purity is easily available while fulfilling the necessary demands.

The tested 5N aluminium strips are cut to measure $(20 \times 200 \times 0.32)$ mm^3. Using equation 3.1 and assuming a thermal conductivity of 100 Wcm^{-1}K^{-1} for the 5N Al, the temperature difference between the two ends of a single strip with a heat load of 1.5 W is approximately 5 Kelvin. Therefore, using multiple strips should provide the necessary thermal conductivity to transmit the cold head's cooling power to the cold bore.

3.7.1 Setup

The basic vacuum chamber and pumping setup presented in 3.4 is kept the same. In addition, a testing structure containing two copper flanges and different configurations of aluminium strips is added. Pictures of this added structure are shown in Figure 25. It is attached to the cold head's sample holder.

For the first testing setup, six strips with the before mentioned dimensions are clamped into two OFHC copper holders. The holders have been annealed for 24 hours at 250 °C before being installed in the setup. The clasps fixing the strips to the holders are made of ordinary copper, but also undergo the same annealing process. The freely hanging holder on the bottom of the strips holds two DT-670 silicon diodes (Diodes 1 and 2) for temperature measurement and two RTO 50 F 22 R heating resistors (Resistors 1 and 2) for supplying heating power.

Each of the Al strips is clasped to the copper holders on either end. The strips are secured by one screw on either side of the strip, pressing down a copper plate onto the strip. A good thermal contact is established by applying a mixture of vacuum grease and silver powder to the contact areas.

The upper copper holder is fixed to the cold head's sample holder as shown in Figure 25 (b). Attached to it are the remaining two temperature sensors (Diodes 3 and 4).

For the second testing setup, most of the elements remain the same as described above. However, a second layer of 5N aluminium strips is added as shown in figure 26. Contacting grease is applied not along the entire length of the strips but only at their ends. In addition, the mixture is also placed on the contacting areas between the strips and the holders.

In a third testing setup, only four Al strips are installed. This is shown in Figure 27 . In addition, the contact medium is exchanged. Not vacuum grease, but a 0.2 x 20 x 20 mm^3 layer of indium is inserted between the copper and the aluminium as well as between the foils. The location of all temperature sensing diodes and heating resistors remain unchanged.

3.7.2 Measurements

The measurements performed with the Al strips are conducted identically for single as well as double layers.

For extracting the thermal conductivity of the aluminium strips, the setup is firstly cooled down to around 5 K via the RDK-408D2 cold head. The temperatures measured during this process are shown in Figure 28 for the single strips and Figure 29 for the double layers. Then, the bottom copper holder is heated with the following input powers: 1.0 W, 2.0 W, 3.0 W and 4.0 W. These are supplied by Resistors 1 and 2 in equal parts, e.g. for 1.0 W of input power, each of the resistors delivers 0.5 W. The temperature measured by the temperature sensors is monitored and recorded using the Lake Shore temperature controller Model 350.

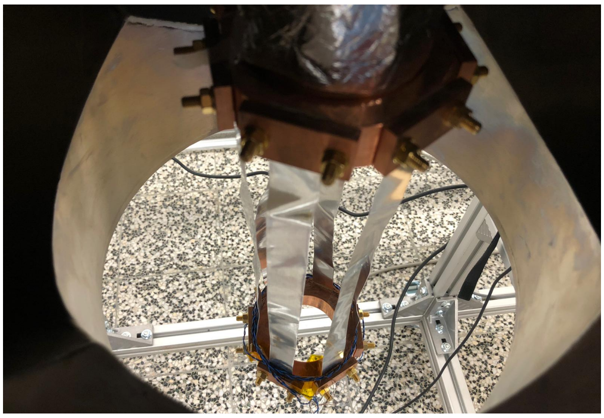

(a) Aluminium strips are attached to two OFHC copper holders.

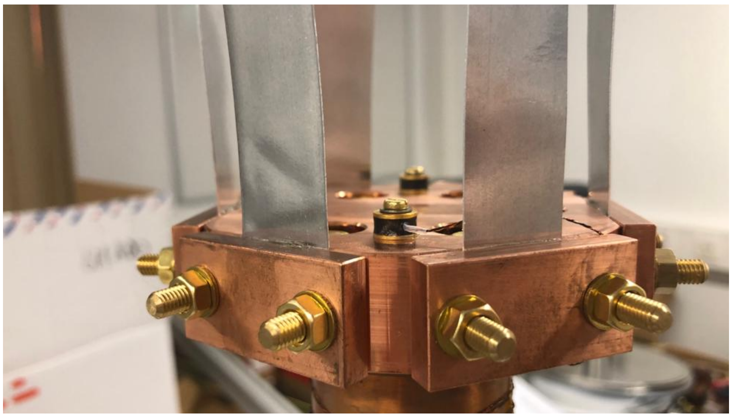

(b) Upper holder connecting to the sample holder of the cold head. Both temperature sensors (Diodes 3 and 4) are clearly visible.

(c) Bottom copper holder including Diodes 1 and 2 and Resistors 1 and 2.

Figure 25: Testing setup for six 5N aluminium strips.

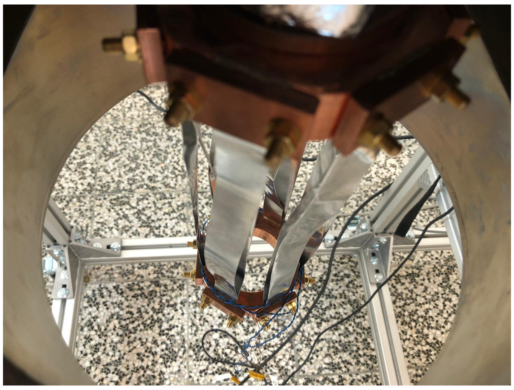

Figure 26: Double Layer of 5N aluminium strips implemented in the testing chamber.

Figure 27: Testing setup using indium as a thermal contact agent.

Each of the measurements is performed over periods of 3 to 10 minutes until the system reaches equilibrium. The measurements are repeated once to check for reproducibility. Examples for temperatures monitored during heating are given in Figure 30.

Two additional measurements using the Al strips are performed. Firstly, the thermal conductivity of the foils, as shown in Figure 27, is measured by supplying the system with heating power as described above. In this setup, the combination of vacuum grease and silver powder used for optimising thermal conductivity has been exchanged for indium. For the second measurement, the foils are forcibly bent and deformed. Then, the setup is again heated with 1.0 W, 2.0 W, 3.0 W and 4.0 W and the resulting thermal conductivity is compared to the one determined for the foil in pristine condition. The cooling curves for both cases are shown in Figure 31 for the unbent and in Figure 32 for the bent foils. Figure 33 shows the measurements with 2.0 W input power for the unbent and deformed strips, respectively.

The method to determine the final temperature recorded by the diodes is identical to the one presented in Section 3.5 using Excel's functions to calculate the mean and standard deviation of the last 100 data points. The thus extracted temperatures for all measurements are listed in appendix A.

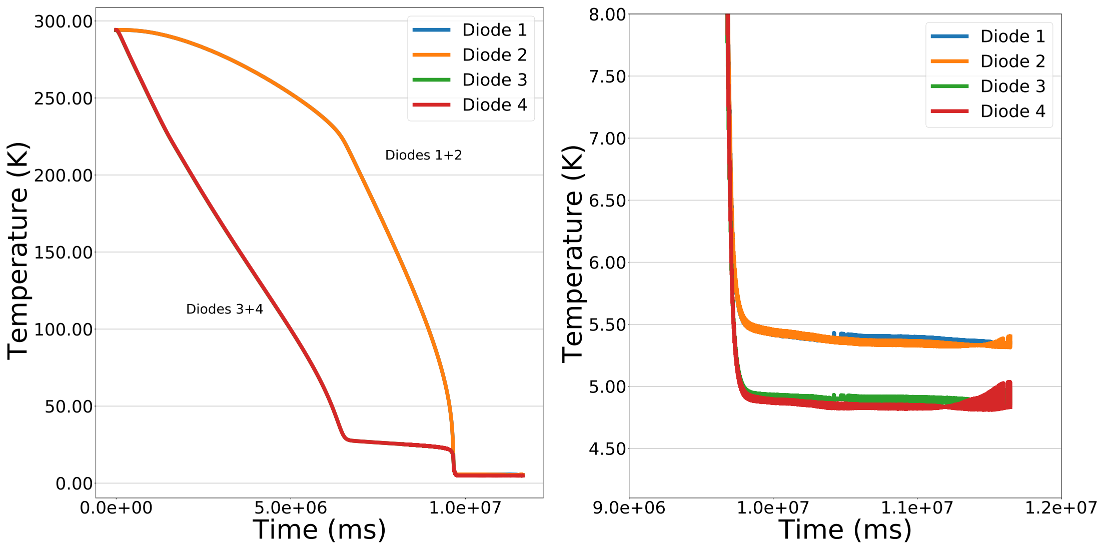

(a) Temperatures measured during the entire cooling process.

(b) Final temperatures reached.

Figure 28: Cooling process of the single 5N Al strip setup.

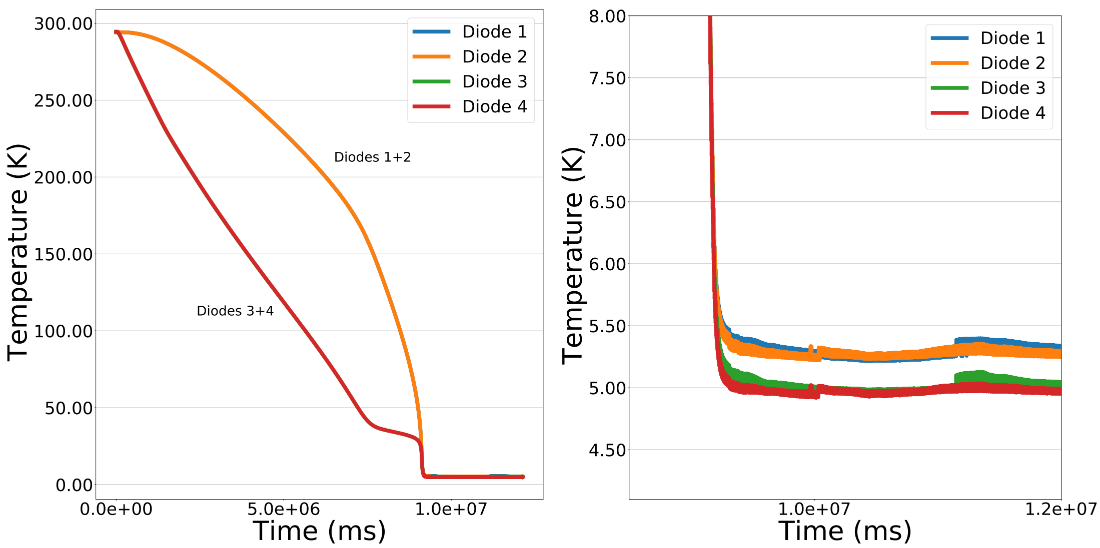

(a) Temperatures measured during the entire cooling process.

(b) Final temperatures reached.

Figure 29: Cooling process of the double 5N Al strip setup.

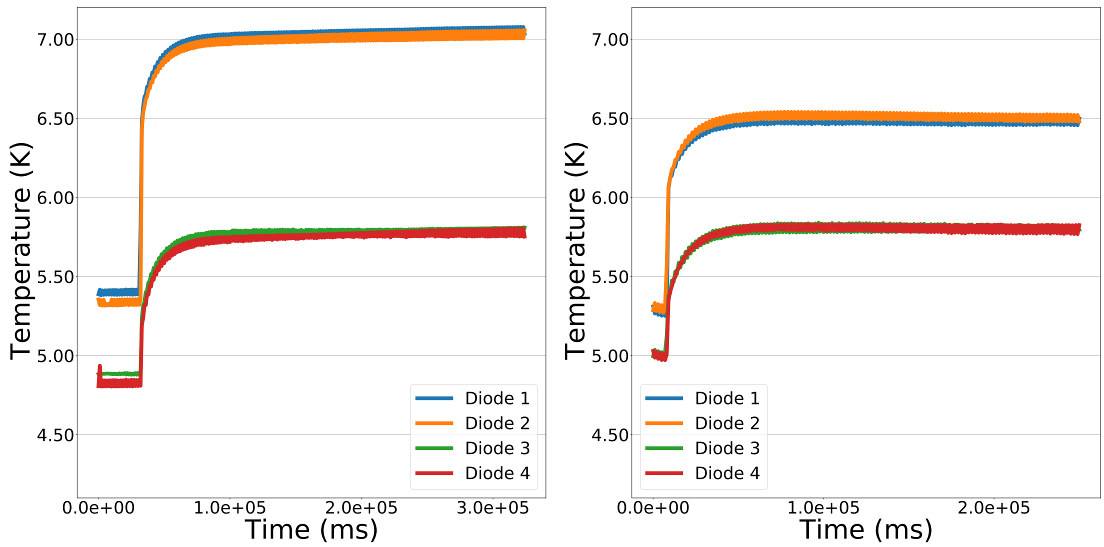

(a) Temperatures measured with a power input of 1.0 W during the single strip testing.

(b) Temperatures measured with a power input of 1.0 W during the double layer testing.

Figure 30: Example temperature measurements for Al strip testing.

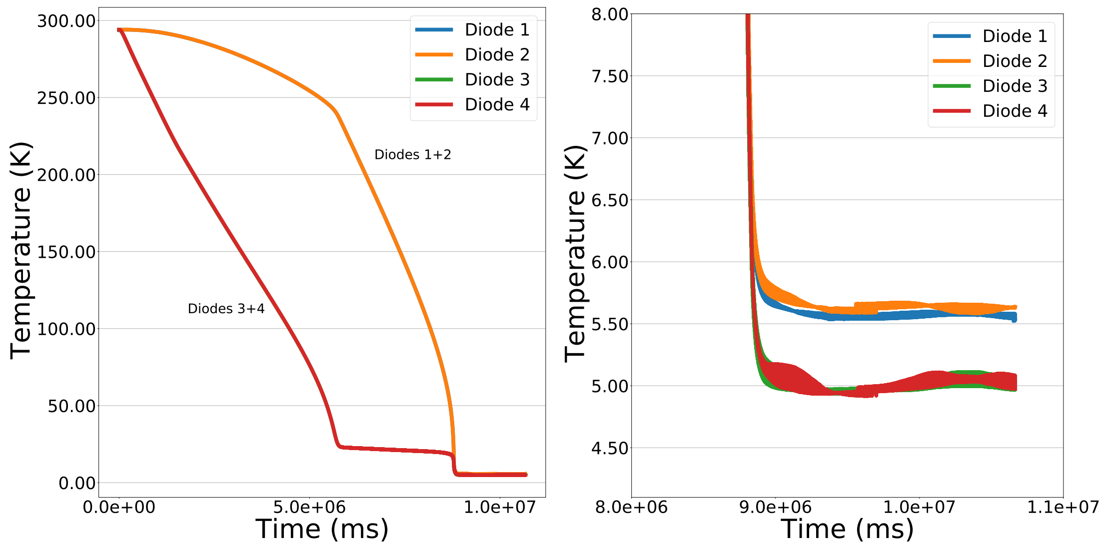

(a) Temperatures measured during the entire cooling process.

(b) Final temperatures reached.

Figure 31: Cooling process of the double aluminium strips using indium as a thermal conductor.

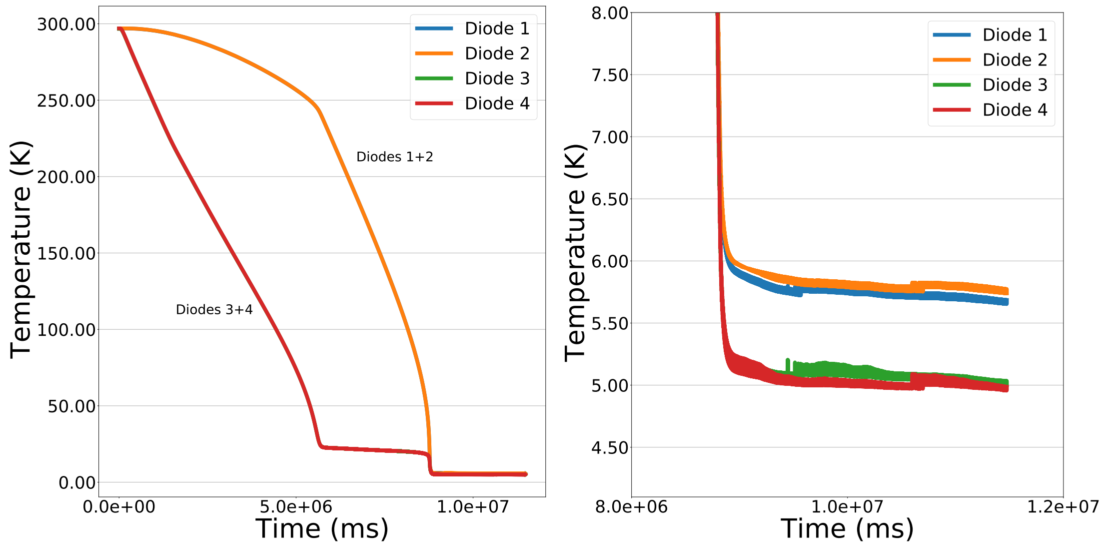

(a) Temperatures measured during the entire cooling process.

(b) Final temperatures reached.

Figure 32: Cooling process of the deformed double aluminium strips using aluminium as a thermal conductor.

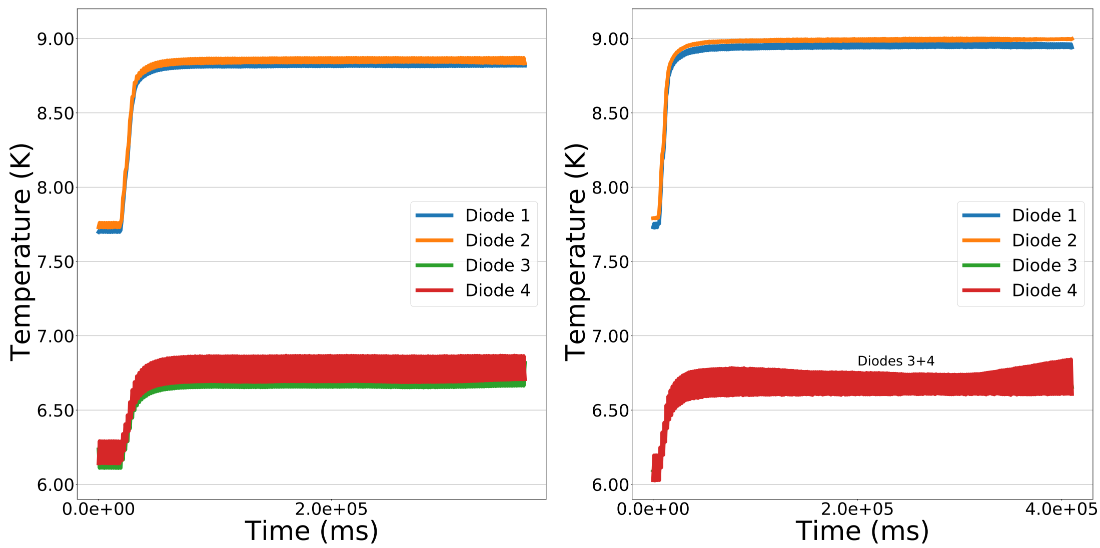

(a) Temperatures measured with a power input of 2.0 W during the unbent strip testing.

(b) Temperatures measured with a power input of 2.0 W during the bent strip testing.

Figure 33: Example measurements for Al strip testing using indium as conducting material.

3.7.3 Results

In order to calculate the thermal conductivity of the aluminium strips, equation 3.1 is used. The input parameters are given in the following:

- q is the power input.
- L is the length of the strips (20 ± 1) cm.
- A is the cross section of the strips. One strip has a cross section of (2.0×0.032) cm^2. Since six strips are used, the total cross section is (0.364 ± 0.011) cm^2 for the single strip measurements. For the double strip tests, the cross section is (0.768 ± 0.064) cm^2 and for the measurements performed with indium the area is (0.256 ± 0.022) cm^2 since only four strips are used.
- ΔT is the temperature difference. Since there are two sensors located on either end of the strips, the mean value between Diodes 1 and 2 on the lower end and Diodes 3 and 4 at the upper end are taken.

Single Layer

The calculated results for the thermal conductivity between the lower and the upper copper holder of the single layer of 5N aluminium strips are shown in Tables 4 and 5 for both measurements, respectively. The combined results are presented in Figure 34. The results of both measurements are in good agreement with each other. The calculated thermal conductivity coefficients of the strips are significantly lower than the ones determined for the 5N aluminium rods in Section 3.5. This might be due to several factors, such as the fact that the strips were slightly bent during their installation into the setup. One should also keep in mind, that the temperature sensors are mounted to the copper holders. The extracted thermal conductivity is therefore a combination of the ones for 5N aluminium and OFHC copper. Still, the resulting conductivity of the strip is sufficient to cool the freely hanging holder to a temperature of around 5.4 K while the holder mounted to the cold head reaches around 5.0 K. The exact temperature differences for the mean values of both measurements for all power inputs are given in Table 6.

Power	λ (Wcm^{-1}K^{-1})
1.0	(44.9 ± 4.2)
2.0	(54.8 ± 4.5)
3.0	(65.2 ± 5.3)
4.0	(76.0 ± 7.2)

Table 4: Results for the thermal conductivity of the single 5N aluminium strips for the first set of measurements. The given error is calculated using propagation of uncertainty.

Power	λ (Wcm^{-1}K^{-1})
1.0	(46.1 ± 4.4)
2.0	(55.9 ± 4.6)
3.0	(72.0 ± 6.7)
4.0	(81.4 ± 7.2)

Table 5: Results for the thermal conductivity of the single 5N aluminium strips for the second set of measurements. The given error is calculated using propagation of uncertainty.

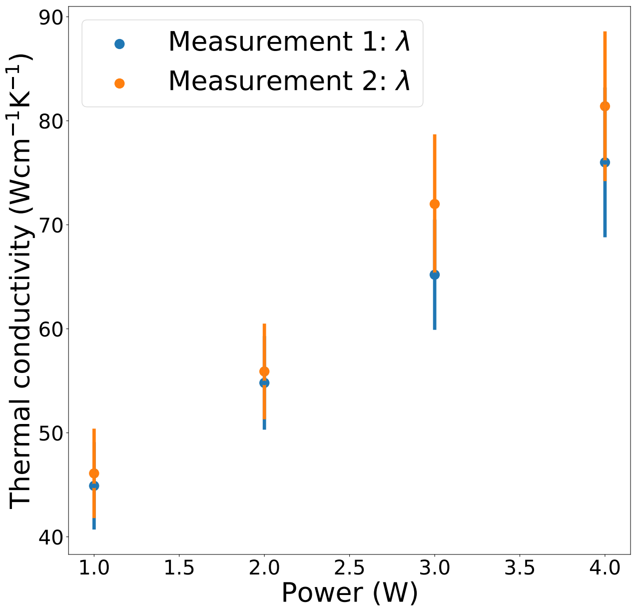

Figure 34: Comparison of the thermal conductivity coefficient of the single Al strips determined by the two data sets.

Power (W)	Temp. Diff. Measurement 1 (K)	Temp. Diff. Measurement 2 (K)
1.0	1.287 ± 0.018	1.255 ± 0.027
2.0	1.734 ± 0.016	1.700 ± 0.025
3.0	2.167 ± 0.070	1.97 ± 0.11
4.0	2.52 ± 0.16	2.35 ± 0.13

Table 6: Temperature differences between the Diodes mounted on upper and lower flanges for the single Al layer measurements. The difference is taken from the mean values of Diodes 1 and 2 on the one hand, and Diodes 3 and 4 on the other. The error is calculated using propagation of uncertainty.

Double Layer

The calculated thermal conductivity coefficients for the testing of the 5N aluminium strips using double layers are given in Tables 7 and 8. The combined results of the two data sets are shown in Figure 35. The results are again in good agreement with each other and with the measurements of the single layers. The temperature differences between the two flanges are shown in Table 9. Comparing them to the values presented in Table 6, they are roughly reduced by half. This reduction of temperature differences between the copper flanges is also clearly obvious in Figure 30. Therefore, the double 5N aluminium layer approach manages to dissipate a higher amount of heat. This makes it a valuable method for ensuring the necessary heat removal from the MREs.

Power	λ ($\text{Wcm}^{-1}\text{K}^{-1}$)
1.0	(42.0 ± 5.3)
2.0	(48.8 ± 5.7)
3.0	(57.5 ± 6.5)
4.0	(70.0 ± 8.6)

Table 7: Results for the thermal conductivity of the double 5N aluminium strips for the first set of measurements. The given error is calculated using propagation of uncertainty.

Power	λ ($\text{Wcm}^{-1}\text{K}^{-1}$)
1.0	(50.8 ± 11)
2.0	(52.2 ± 6.5)
3.0	(59.7 ± 6.9)
4.0	(81 ± 13)

Table 8: Results for the thermal conductivity of the double Al strips for the second set of measurements. The given error is calculated using propagation of uncertainty.

Power (W)	Temp. Diff. Measurement 1 (K)	Temp. Diff. Measurement 2 (K)
1.0	0.689 ± 0.022	0.569 ± 0.097
2.0	0.973 ± 0.025	0.911 ± 0.046
3.0	1.230 ± 0.042	1.184 ± 0.049
4.0	1.366 ± 0.087	1.18 ± 0.15

Table 9: Temperature differences between the Diodes mounted on upper and lower flanges for the double layer measurements. The difference is taken from the mean values of Diodes 1 and 2 on the on hand, and Diodes 3 and 4 on the other. The error is calculated using propagation of uncertainty.

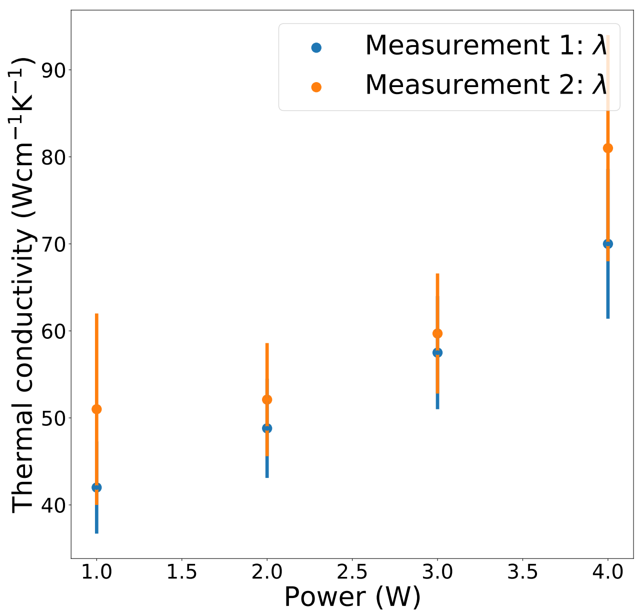

Figure 35: Comparison of the thermal conductivity coefficient of the double layered Al strips determined by the two data sets.

Power	λ ($Wcm^{-1}K^{-1}$)
1.0	(58.3 ± 7.3)
2.0	(68.4 ± 8.0)
3.0	(79.7 ± 8.7)
4.0	(82.4 ± 8.9)

Table 10: Results for the thermal conductivity of the first set of data taken with indium as a conductor.

Power	λ ($Wcm^{-1}K^{-1}$)
1.0	(55.2 ± 6.7)
2.0	(68.3 ± 8.0)
3.0	(79.3 ± 9.0)
4.0	(82.5 ± 9.4)

Table 11: Thermal conductivity of the second measurement taken with indium as a conductor.

Indium conductor

The measured temperatures for two double layered aluminium strips using indium as the conducting material are given in Appendix A. These are calculated using the methods described above. The thus resulting thermal conductivity is given in Tables 10 and 11 for the first and second measurement, respectively. The combined results are presented in Figure 36. The results show an excellent level of agreement. Still, the results clearly indicate that the installation of indium as a thermal conductor does not vastly improve the calculated conductivity. As a result, the combination of vacuum grease and silver powder will be employed for optimising thermal conductivity in the new ASACUSA cold bore since the handling of the indium sheets poses quite a challenge.

Deformed Strips

Keeping the setup shown in Figure 27 the same but forcibly bending and deforming the strips should lower the thermal conductivity. This is due to the resulting irregularity in the metal's lattice. The temperatures measured while heating with 1.0, 2.0, 3.0 and 4.0 W are presented in Appendix A. This time, three sets of measurements are taken. The results are presented in Tables 12, 13 and 14. The combined results for all three measurements are shown in Figure 37. When comparing these to the calculated thermal conductivity of the unbent strips, it appears to be slightly reduced but no radical difference can be established. This is especially important, as their installation in the experimental area will certainly lead to slight mishandling.

Power	λ ($Wcm^{-1}K^{-1}$)
1.0	(49.7 ± 7.9)
2.0	(62.6 ± 7.2)
3.0	(69.5 ± 8.3)
4.0	(71.5 ± 8.6)

Table 12: Calculated thermal conductivity of the first set of data taken for the deformed Al strips.

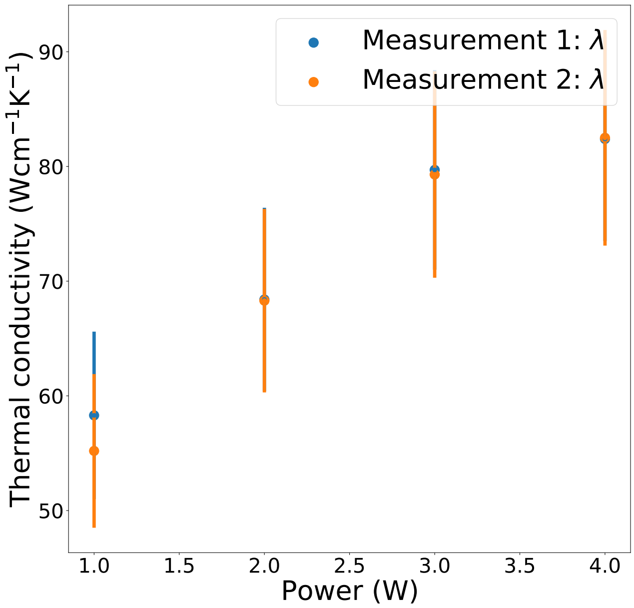

Figure 36: Comparison of the thermal conductivity coefficient calculated for the tests using indium as a thermal conducting material.

Power	λ (Wcm^{-1}K^{-1})
1.0	(55.7 ± 7.0)
2.0	(62.2 ± 7.2)
3.0	(74.9 ± 8.3)
4.0	(80.1 ± 8.6)

Table 13: Calculated thermal conductivity of the second set of data taken for the deformed Al strips.

Power	λ (Wcm^{-1}K^{-1})
1.0	(52.2 ± 6.4)
2.0	(61.7 ± 7.0)
3.0	(70.6 ± 7.7)
4.0	(78.5 ± 8.7)

Table 14: Calculated thermal conductivity of the third set of data taken for the deformed Al strips.

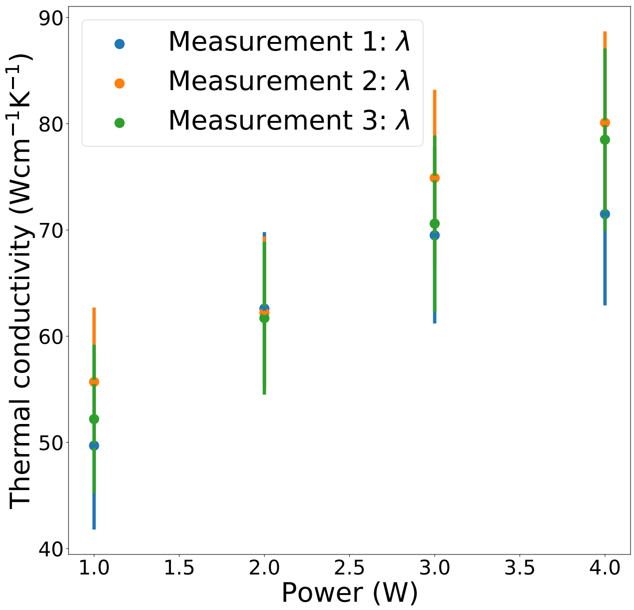

Figure 37: Comparison of the calculated thermal conductivity for the bent 5N aluminium strips.

3.8 Conclusion and Outlook

During this project, the most important elements of the new ASACUSA cold bore have been tested for their thermal conductivity.

For the central element of the cold bore, the 5N aluminium rods, the results are in good agreement with the literature. Therefore, their performance should guarantee a cooling of the MREs to temperatures below 10 K.

The tested bellow shows a high temperature gradient between cooled and heated sides. A temperature rise of about 20 Kelvin on the warm end resulted in a rise below 1 K on the cold end. Therefore, it can be concluded, that a combination of two bellows on either side of the bore should ensure a thermal decoupling between the room temperature and the below 10 K elements.

Finally, the 5N aluminium strips were tested. The calculated thermal conductivity is satisfactory. In addition, several arrangements of foils have been tested. As a result, a double layer of foil will be used for improved heat removal. The mixture of vacuum grease and silver powder will be employed to ensure excellent thermal conductivity between all necessary areas. It has also been shown that bending the strips might decrease the conductivity slightly. However, no drastic change could be observed.

The installation of the new cold bore into the ASACUSA experiments is planned for summer 2021. However, before it is sent to CERN, it first will be assembled in Vienna and a final tests are planned to be performed at SMI.

4 Kaonic Deuterium Experiments

This section discusses two experiments investigating the $2p \rightarrow 1s$ transition in kaonic deuterium, E57 at J-PARC and SIDDHARTA-2 at DAΦNE. Firstly, a brief introduction to the field of kaonic atoms is given. Secondly, both experiments are discussed regarding their design and the measurements performed for this thesis.

4.1 Introduction

4.1.1 Kaonic atoms and QCD Studies

In exotic atoms a negatively charged particle other than an electron – mesons, antiprotons, muons, etc. – is bound to the atomic nucleus by the electromagnetic force. Such systems were first theoretically proposed in the 1940s (e.g. [32]). In kaonic atoms, the electron is replaced by a negatively charged kaon (K^-). Since kaons are made of quarks and therefore belong to the hadron family, they not only interact with the nucleus via the electromagnetic but also by the strong interaction. The latter is described by quantum chromodynamics (Quantum ChromoDynamics (QCD)). However, not only their mode of interaction is of significance. K^- particles are a bound state of anti-up ($\bar{u}$) and strange (s) quarks. As a result, kaonic atoms present the perfect environment for studying low-energy QCD involving strangeness.

A kaonic atom is formed when a kaon with a kinetic energy of a few eV is captured in the outer shell of an atom, replacing one of its electrons. The significant mass difference between electrons (0.5 MeV/c^2 [33]) and kaons (493.7 MeV/c^2 [33]) results in the kaon being captured in a highly excited state.

Due to the high principal quantum number of $n \sim 25$ of the captured kaon, it begins to cascade towards lower energies. The dominant processes during this cascade depend on the atomic number of the system. For kaonic hydrogen and deuterium Stark mixing, Coulomb de-excitation, the Auger effect, and at lower energies radiative decay form the most prominent ones [34].

Since K^- interact with the nucleus not only via the electromagnetic but also via the strong interaction, the $1s$ state in kaonic atoms experiences a broadening – denoted by the observable Γ– and a shift – ε – with regard to its electromagnetic value. The latter can be calculated using the Klein-Gordon equation. Thus, the observed shift ε_{1s} results in comparison of the energy of the K_α X-ray transition of electrons and kaons:

$$\varepsilon_{1s} = E_{2p \rightarrow 1s, measured} - E_{2p \rightarrow 1s, electromagnetic} \tag{4.1}$$

The strong interaction's influence on the $1s$ state also produces a broadening of the state's width Γ_{1s} due to opened reaction channels which reduce the lifetime τ of the low-angular-momentum states [34].

In order to verify competing theoretical approaches and introduce necessary constraints, experimental data of low-energy QCD systems are needed. This can be accomplished by providing measurements regarding the isospin-dependent antikaon nucleon ($\bar{K}N$) complex scattering lengths a_0 ($I = 0$, isoscalar) and a_1 ($I = 1$, isovector) of the s-wave for the system at rest. They are related to the observable shift ε_{1s} and width Γ_{1s} via:

$$\Delta\varepsilon_{1s} - \frac{1}{2}\Gamma_{1s} = -2\alpha^3\mu^2 a_{K-d}(1 - 2\alpha\mu(ln(\alpha) - 1)a_{K-d})) \tag{4.2}$$

which is a modified version of the Deser-Trueman formula ([35, 36]) formulated for mesonic atoms [37]. This improvement for kaonic atoms was necessary as the isospin-breaking terms are much larger than in pionic atoms [38].

Experiment	ε_{1s} (eV)	Γ_{1s} (eV)	Reference
KpX	-323 $\pm$ 74	407 $\pm$ 308	M. Iwasaki et. al. [40]
DEAR	-193 $\pm$ 43	249 $\pm$ 141	G. Beer et. al. [41]
SIDDHARTA	-283 $\pm$ 42	541 $\pm$ 101	M. Bazzi et. al. [42]

Table 15: Results from experiments measuring K_α X-rays of kaonic hydrogen. Errors represent the sum of statistical and systematical errors.

The complex scattering lengths (a_0, a_1) can be calculated from the scattering lengths $(a_{K^-p}, a_{K^-d}, a_{K^-n})$ determined for the K^-p and K^-d systems using the following relations:

$$a_{K^-p} = \frac{1}{2}[a_0 + a_1] \tag{4.3}$$

$$a_{K^-n} = a_1 \tag{4.4}$$

$$a_{K^-d} = \frac{4[m_N + m_k]}{2m_N + m_K} Q + C \tag{4.5}$$

where C encompasses the higher-order effects resulting from the K^-d three body process and the first term of 4.5 including

$$Q = \frac{1}{2}[a_{K^-p} + a_{K^-n}] = \frac{1}{4}[a_0 + 3a_1] \tag{4.6}$$

represents the lowest-order process, meaning the K^- scattering on both nucleons [39].

Experiments extracting the kaonic hydrogen scattering length (a_{K^-p}) have been done at the National Laboratory of Frascati (LNF) in Italy and the proton synchrotron at High Energy Accelerator Research Organization (KEK) in Japan. A comparison of the results of the three kaonic hydrogen experiments is shown in Table 15 and in Figure 38.

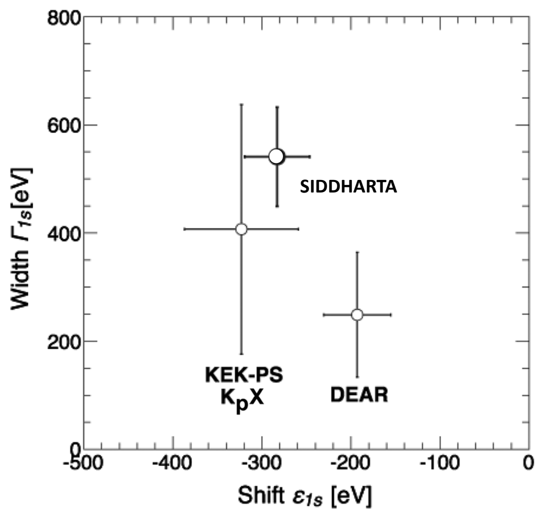

Figure 38: Results of shift and width of the kaonic hydrogen $1s$ state from experiments KEK-PS KpX [40], DAΦNE Exotic Atoms Research (DEAR) [41] and SIDDHARTA [42] with error bars being quadratically added statistical and systematic errors. *Picture adapted from [39].*

4.1.2 Kaonic Deuterium Experiments

As already explained in section 4.1.1, kaonic deuterium measurements are necessary in order to extract the isospin dependent scattering lengths a_0 and a_1. Therefore, two new experiments were developed, SIDDHARTA-2 at DAΦNE as well as E57 at J-PARC. The following sections will present the details of their respective working principles as well as the tests performed for this thesis.

The most important restricting factor for measuring the shift and width of the $1s$ state is the very low X-ray yield $Y_{K-d} \sim 0.2\%$ which is around one order of magnitude lower than the yield of kaonic hydrogen [43]. In addition, the $1s$ width is expected to be a factor 2 larger in kaonic deuterium resulting in faster absorption of the kaon by the nucleus. Another important aspect is the high radiation background of the accelerator environments of these experiments. In order to optimise the two experiments for X-ray spectroscopy with good background suppression, the following requirements need to be fulfilled [39, 44]:

1. *Large X-ray detector*: Newly developed SDD cells with large active area which are arranged around the target cell. They have excellent timing (300 ns) and energy resolution (150 eV).

2. *Lightweight cryogenic target*: A target made out of two 50 μm layers of kapton foils connected by epoxy glue ensures 90% transmission of the K_α X-rays. In addition, a gas density of 3-4% was found to be optimal.

3. *Veto-system*: A dedicated detector system is needed for suppression of background by discarding irrelevant events. Excellent timing resolution would provide the means to distinguish between kaons stopped in the deuterium gas and kaons stopped in other parts of the setup.

The remaining part of this thesis is concerned with points 1 and 2 and their implementation at SIDDHARTA and E57.

4.2 The E57 Experiment at J-PARC

4.2.1 Setup at J-PARC

The E57 experiment is performed at the K1.8BR beam line at the hadron hall of the J-PARC facility in Japan. A schematic drawing of the experimental area is shown in Figure 39.

A primary beam of protons with an energy of 50 GeV is supplied by the J-PARC proton synchrotron (PS) and focused onto a production target. The outgoing beam of secondary particles passes through a beam line spectrometer. There, particles with a momentum in the region of 0.9 GeV/c to 1.2 GeV/c are extracted and kaons and pions are distinguished by a kaon identification trigger [45].

The by-products of the interactions in the target area are detected by a Cylindrical Detector System (CDS) consisting of a solenoid magnet with a 0.7 T magnetic field, a Cylindrical Drift Chamber (CDC), and a Cylindrical Detector Hodoscope (CDH). Together, the CDC and CDH result in a coverage of 59% of 4π and provide particle identification as well as background suppression by determining the origin of a tracked particle [45].

A preliminary design of the E57 target cell is shown in Figure 40 (a). The lightweight target cell is surrounded by a layer of SDD X-ray detectors. They are then placed in the centre of the CDS solenoid. Two cold heads are used in order to cool down the target to 30 K while the SDDs remain at 120 K. Due to the geometry of the experiment, the necessary cold head is placed at an 90° angle to the target [39].

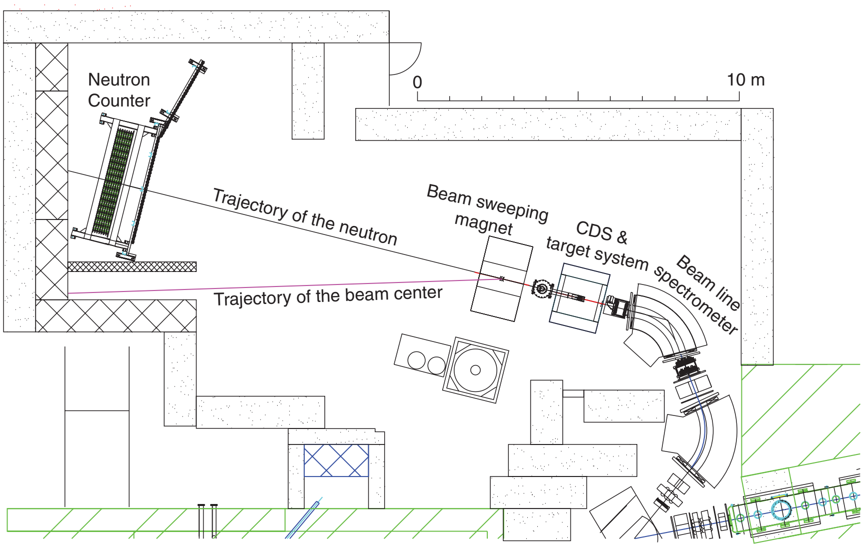

Figure 39: Schematic drawing of the K1.8BR beamline at J-PARC. *Picture taken from* [45].

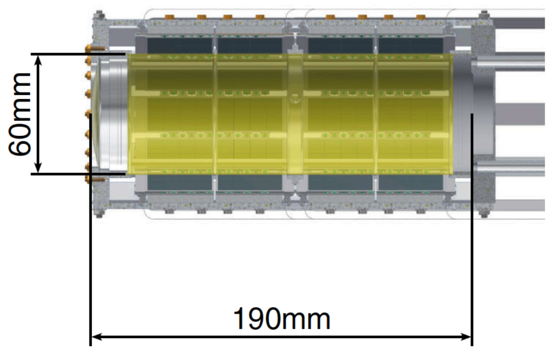

(a) Sketch of E57 target cell.

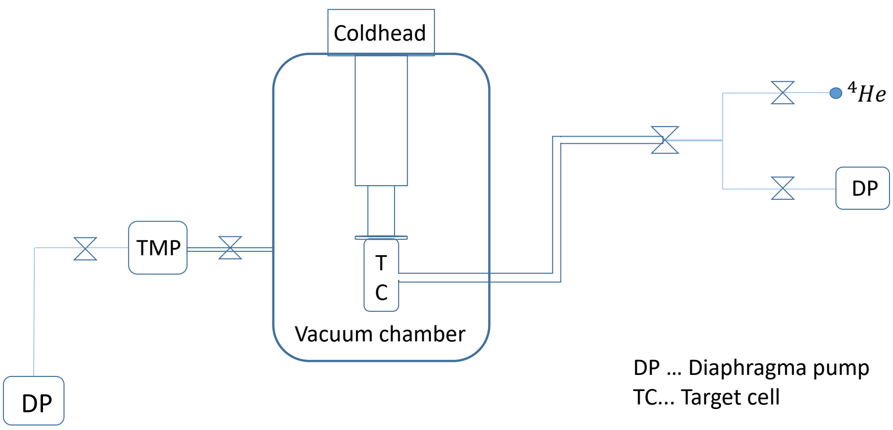

(b) E57 setup including CDS.

Figure 40: Layout of the E57 target cell and setup. *Both pictures taken from [39].*

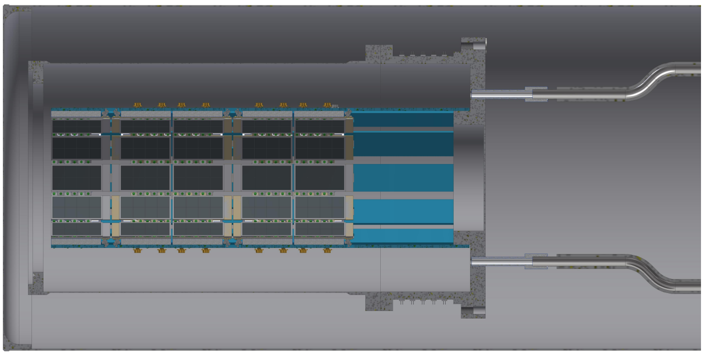

Figure 41: New active target design of the E57 target cell. *Courtesy of: D. Pristauz-Telsnigg.*

4.2.2 New Target Cell Design

During the last test beam time of the experiment in 2019, the measured kaonic hydrogen X-ray rate produced by the $2p \rightarrow 1s$ transition was much lower than expected [46]. As a result, it was decided that the original design shown in Figure 40 needs to be updated to an active target. This new design is shown in Figure 41. The fundamental change is the location of the SDD X-ray detectors. Instead of being mounted concentrically around the target cell, they will be placed inside the target walls. Since the X-rays do no longer need to transition through the walls to reach the SDDs, the new target will be made entirely of metal.

As a result, the demand for a cryogenic feed through system for the X-ray detector electronics arises. The most important factor in its design is minimising the leak rate of deuterium into the vacuum. In order to ensure the tightness of the cell, a sealant of Aremco-bond 2310 type is chosen. It has been tested to ensure a minimal leak rate at room temperature as well as at 130 K.

4.2.3 Setup at SMI

This section discusses the test setup for the J-PARC target cell at SMI. A sketch of the layout and a picture of the used vacuum chamber are shown in Figure 42. The setup consists of a vacuum chamber containing the target cell. Using a vacuubrand diaphragm and the Edwards nEXT240D 160WvTMP, a pressure of around $5 \cdot 10^{-6}$ mbar at room temperature and $3 \cdot 10^{-6}$ mbar after cooling is produced. The cooling system used is a Cryotiger cold head and the corresponding PCC compressor, reaching a minimum of 70 K and producing a cooling power of 0.5 to 30 W depending on refrigerant and other operating conditions [1]. Using PT-14 as the working gas, a final temperature of around 150 K is measured for this setup using two PT-100 temperature sensing resistors. They are connected to a Lake Shore model 335 in order to display the temperature of the target cell.

The target itself is made up out of a metal cylinder, the top of which can be attached to the cold head's sample holder on one end via a metal clasping mechanism. On the opposite end the feed through flange can be exchanged in order to make testing of different feed throughs possible. The target cell is shown in Figure 44. On the left hand side the sample holder of the cold head wrapped in superinsulation is visible. One of the two PT-100 temperature sensors attached to the cell is also captured. The second sensor is located on the opposite side of the target.

The tested elements are shown in Figure 43. The cap assigned number 1 consists of kapton foil with an inlay of electric conductors. Feed through number 2 is made up of plastic printboard material. Due to the tests being focused on leak rate, the target was connected to a helium 4.6 bottle and a second vacuubrand diaphragm pump via a valve system, making

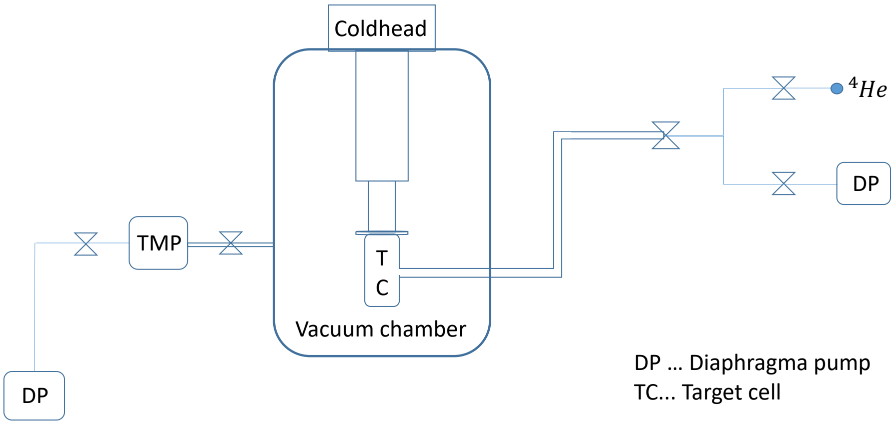

(a) Layout of test setup

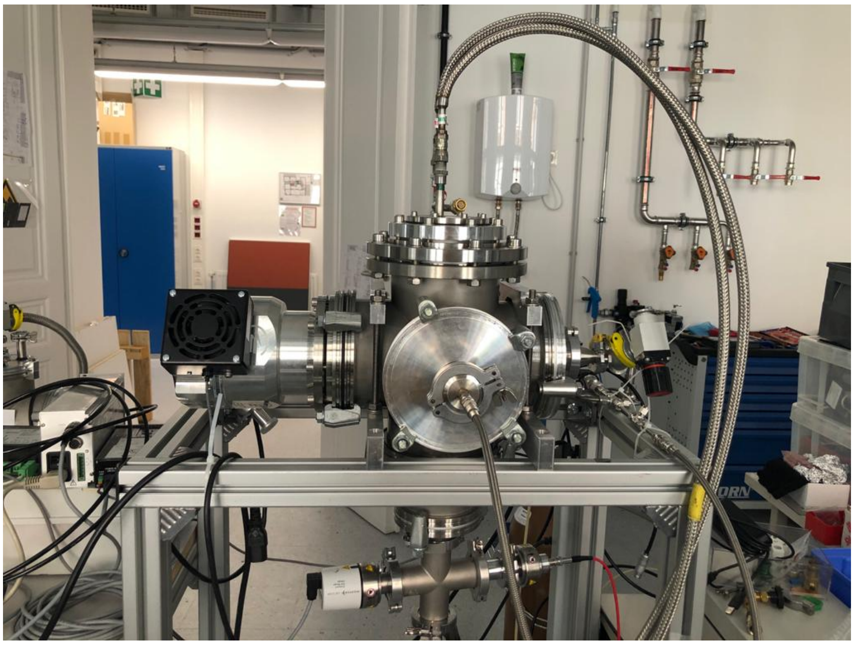

(b) Vacuum chamber used for test setup

Figure 42: Setup at SMI for E57 target cell tests.

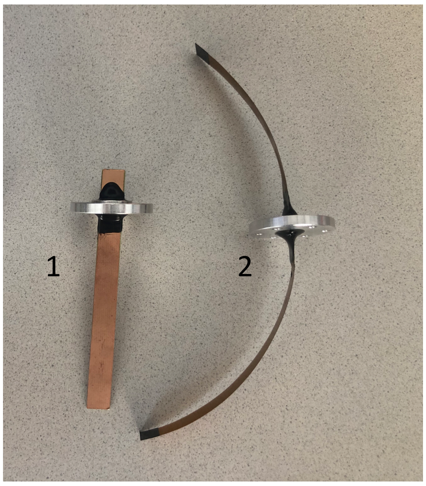

Figure 43: Tested feed throughs.

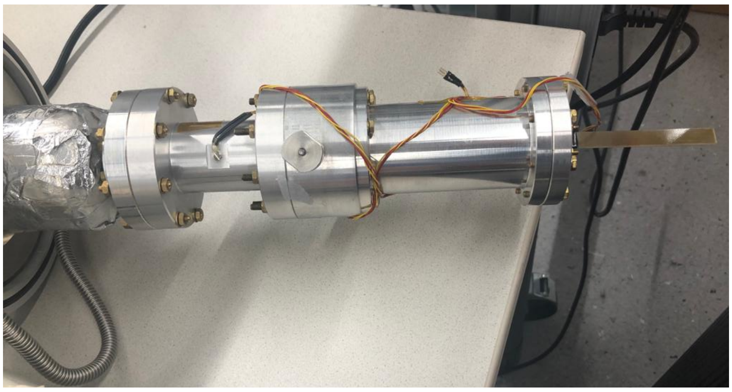

Figure 44: J-PARC target cell.

filling and emptying of the cell easily accomplishable.

In order to establish the leak rate of the target cell, a Pfeiffer HLT57 leak detector is used. After establishing vacuum in the chamber, it is attached to the structure instead of the diaphragm pump before the TMP. In order not to disturb the vacuum during this process, the valve between the diaphragm pump and TMP is closed and only reopened after the evacuation of the tube connecting the leak detector to the vacuum chamber.

4.2.4 Measurements and Results

Kapton Feed Through

One of the possible feed through materials for the J-PARC target cell is kapton foil with integrated lines for the SDD electronics (number 1 in Figure 43). Indium is used as a sealing agent between the feed through flange and the rest of the target cell. After cooling the system down to about 140 K, the target was filled to a pressure of

$$p_{target} = (0.92 \pm 0.01)\ \text{bar}$$

This resulted in a leak rate of

$$L = (1.1 \pm 0.2) \cdot 10^{-8}\ \text{mbar} \cdot \text{l/s}$$

The uncertainty of the pressure is taken to be the systemic error of the used pressure display. The error stated for the leak rate is 15% as stated by the manufacturer.

Printboard Feed Through

Another possibility to be considered are print boards working as feed throughs, pictured in Figure 43 as number 2. Again, indium is used as a sealing agent between the cap and remaining target. Cooling the system down and filling the cell with helium to a pressure of

$$p_{target} = (1.08 \pm 0.01)\,\text{bar}$$

produces a leak rate of

$$L = (3.1 \pm 0.5) \cdot 10^{-9}\,\text{mbar} \cdot \text{l/s}$$

The uncertainties stated here are determined in the same way as above.

As obvious by these measurements, the leak rate of the print board version is almost a factor 10 better than the one measured for the kapton foil. Therefore, it can be concluded that plastic print board feed throughs provide the properties necessary for the construction of an active deuterium target.

4.2.5 Conclusion and Outlook

Two possible materials for the new active target cell design for the E57 experiment at J-PARC have been tested. Due to the significantly better results for the print board version, this material has been chosen to be implemented as the method of feeding through the SDDs' electronics.

However, before finalising the design a prototype using a single final print board will be constructed and tested at SMI. After establishing the leak rate of this single feed through, a target cell encompassing feed throughs for all employed SDD arrays will be built and tested at SMI.

4.3 The SIDDHARTA-II Experiment at DAΦNE

4.3.1 Setup DAΦNE

Just like its predecessor SIDDHARTA, the SIDDHARTA-2 experiment is located at the e^+e^- collider DAΦNE at the LNF. This collider complex is made of two rings in which the electrons and positrons circulate in opposite directions with one interaction points for experiments. The collider operates at a centre of mass energy of 1.02 GeV, the equivalent of the rest energy of the Φ-meson [47]. Since the dominating decay mode of the meson is $\Phi \rightarrow K^+K^-$ with about 50$\%$ [33], a monoenergetic kaon beam is produced.

A schematic drawing of the SIDDHARTA-2 setup is shown in Figure 45. The experiment is located right above the e^+e^- interaction point of the DAΦNE collider. The back to back emitted kaons are registered by a kaon trigger system located above and below the beam line. The target cell is fixed inside a vacuum chamber. A sketch of the target is shown in Figure 46. It is surrounded by 48 SDD arrays which are mounted directly onto the target cell via 24 aluminium plates. Behind the X-ray detectors, the Veto-2 system is located. This system of scintillating tiles and Silicon PhotoMultiplier (SiPM) read-outs is used to suppress hadronic background in the SDDs spectra. The other veto system (Veto-1) is mounted outside the

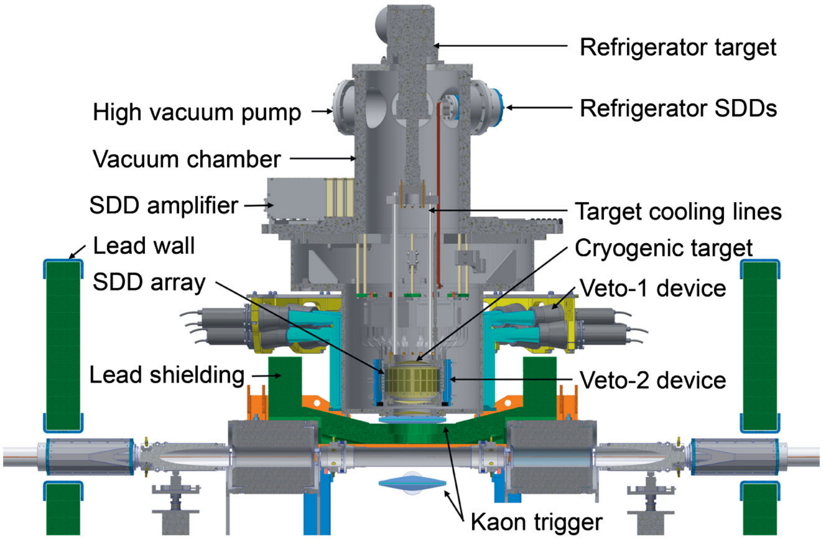

Figure 45: Schematic drawing of the SIDDHARTA-2 setup. *Picture taken from* [39].

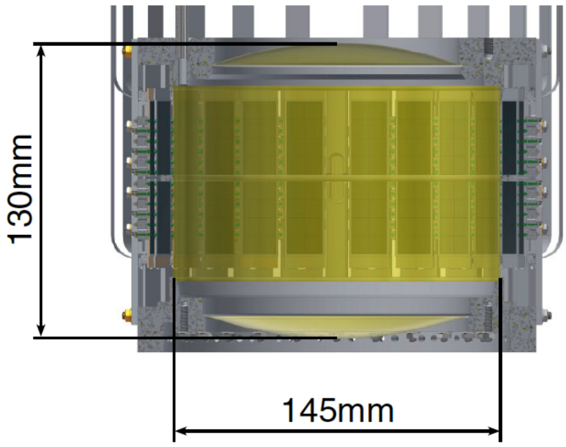

Figure 46: Sketch of the SIDDHARTA-2 target cell. *Picture taken from* [39].

vacuum chamber and determines the location of a kaon stop based on timing information. It consists of a barrel of scintillators and Photo Multipliers (PMs) acting as read-outs. [39]

First experimental runs have shown that the target cell design is not optimal for the used SDD units. As shown in Figure 48 the SDDs are glued down onto ceramic holders with electronic inlays which provide the necessary voltage to the X-ray detectors. However, the used adhesive has been found to break down at very low temperatures (70 K or lower). As a result, new techniques are demanded in order to maintain the SDD units at an optimal temperature of 120 K [48].

4.3.2 Setup at SMI

A sketch and a photo of the testing setup at SMI are shown in Figure 47.

For producing the necessary vacuum conditions, a system of one scroll pump (Leybold Scrollvac 7 plus) and one TMP (Pfeiffer TC 400 PB) is used. As a result, a pressure of $2 \cdot 10^{-6}$ mbar is reached at room temperature. After the cooling process, the pressure is reduced to around $6 \cdot 10^{-7}$ mbar.

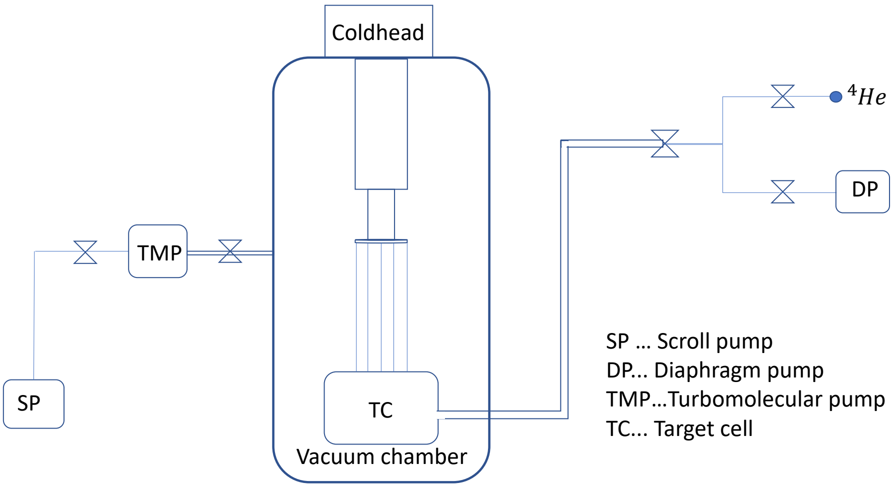

(a) Layout of the SIDDHARTA-2 target cell setup at SMI.

(b) Photo taken of the SIDDHARTA-2 target cell testing chamber.

Figure 47: Setup for the SIDDHARTA-2 target cell tests.

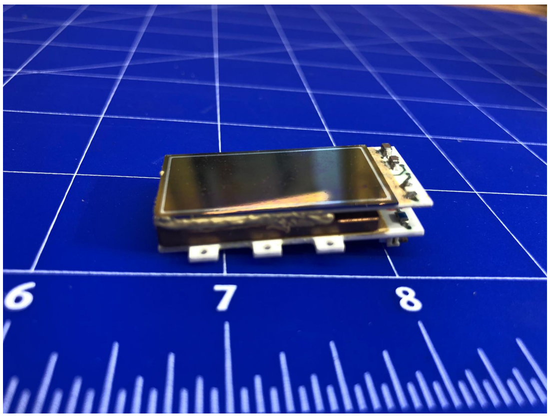

Figure 48: The SDD X-ray detectors used for SIDDHARTA-2 and E57.

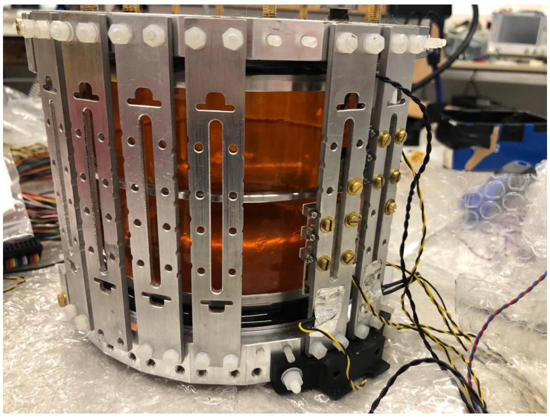

Figure 49: The SIDDHARTA-2 testing target cell.

The cryogenic temperatures are reached using a G-M type cooling system. The cold head is the Coolpower 10 MD and the corresponding compressor is of the model Coolpak 6000H both of which are produced by Leybold.

The target cell is mounted to a structure of four 50 cm high purity aluminium bars connecting the target to the sample holder of the cold head. This simulates the setup at the DAΦNE collider as shown in Figure 45. A mixture of vacuum grease and silver powder is applied to the contact areas between the aluminium structure, the sample holder on one side, and the target cell on the other. This ensures excellent thermal conductivity between these elements. One DT-670 silicon diode is mounted to either end of the Al rods. They are read out using a Lake Shore model 335. The temperatures are recorded using the software provided by the manufacturing company.

A photo of the installed target cell is shown in Figure 49 (a). It is mostly made out of two layers of kapton foil with a thickness of 50 μm each, held together by an epoxy adhesive. The form giving parts of the cell are made from aluminium. The kapton walls and the surrounding 24 aluminium plates are clearly visible. In the final SIDDHARTA-2 setup these would hold the X-ray detectors. In order to minimise the thermal conductivity between target and the aluminium plates, the latter are mounted to the cell structure via headless screws, washers, and nuts which are all made out of nylon instead of metal.

During the first tests, several different elements are mounted onto the aluminium plates:

- Two SDD dummies are installed. They consist only of the ceramics and the electronic inlays. They simulate real SDDs and provide information on the possible SDD temperatures using the tested techniques. The dummies are located on Plates 1 and 2 and face towards the target's centre as they simulate X-ray detectors.

- Five temperature sensors are installed in order to monitor temperature changes on the Al plates. The employed sensors are PT-1000 resistors. A single sensor (PT5) is located on Plate 13. Plate 1 holds two sensors. One (PT1) is mounted onto the SDD dummy, while the second (PT2) is fixed to the backside of the plate. Two more sensors (PT3 and PT4) are mounted in similar fashion to Plate 2 with the second dummy. They are read out using the PT-104 Platinum Resistance Data Logger by Pico Technology. The data of the sensors is recorded in form of resistance using the software provided by the manufacturer. The temperatures are calculated in the final step by using the "pt1000_temperature" function in the UliEngineering.Physics.RTD python package [49].

- Six resistors are implemented for introducing heating power to the plates surrounding the target. They are of the type RTO 50 F 22 R with a $\pm 5\%$ tolerance. A GW Instek GPD-4303S power supply is used for providing voltage and current. The resistors are mounted onto Plates 1, 2, 5, 11, 17, and 22.

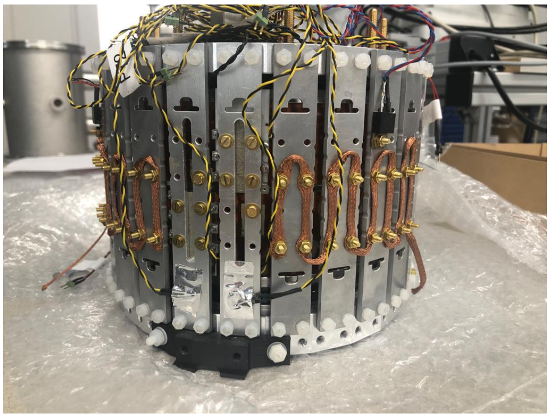

(a) Close up photo of the target cell.

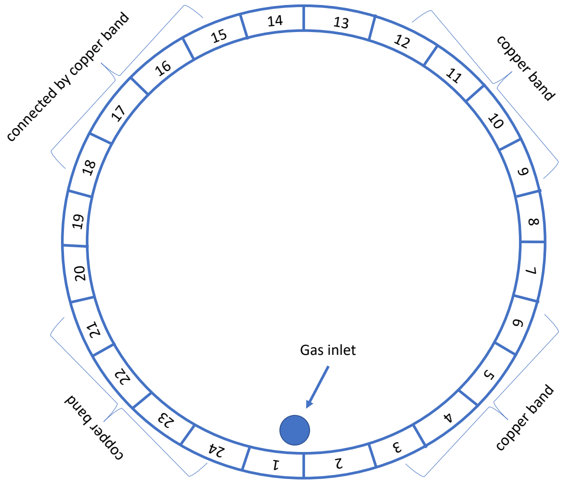

(b) Sketch of the target cell and the 24 Al plates including the location of the cell's gas inlet and the copper band connections visible in (a).

Figure 50: The SIDDHARTA-2 target cell prepared for the first measurement.

- Four 30 cm copper bands connect four neighbouring plates each around the target: Plates 3-6, 9-12, 15-18, 21-24. They are fixed to the Al plates via brass screws and nuts for establishing good thermal contact. They distribute the heating induced by the resistors to all connected plates.
- Two plate designs are used: Plates 1, 2, 13, and 14 have slits at their centre. The rest have no such cut-outs.

The picture taken of the target with all these elements already installed is shown in Figure 50. There, the difference between the two plate designs is also clearly visible.

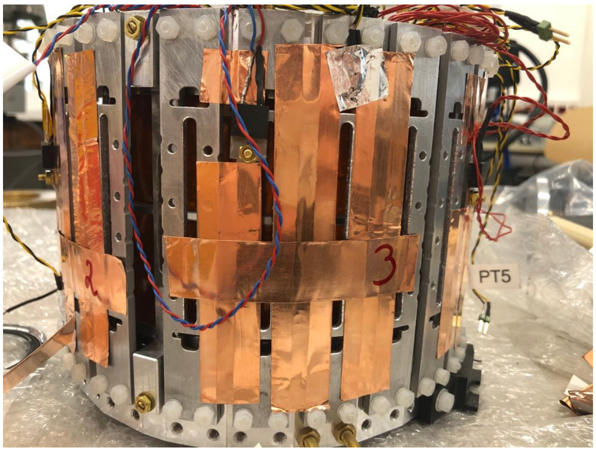

Figure 51: The SIDDHARTA-2 target cell prepared for the second test measurement.

For the second testing arrangement, the elements on the target cell are modified as presented in the following:

- The plates now all have the same shape. A slit has been cut into all 24 plates to reduce thermal conductivity.
- The SDD dummies are removed to produce uniform conditions around the entire target cell.
- Four neighbouring plates are connected. As a result six groupings are formed. One such cluster is shown in Figure 51. The four Al plates are thermally connected using strips of copper tape. On one of the centre plates, a single heating resistor is placed. The same kind as described above is used. The temperature of one entity is measured by a single PT-1000 sensor. The placement of the sensor varies from unit to unit in order to compare the temperature change for different locations and distances from the resistor.

In order to minimise the impact of thermal radiation on the setup, the entirety of target cell, aluminium rods and cold finger is wrapped in several layers of super insulation.

Since these measurements are performed to simulate the conditions at the final experimental setup, the input power should correlate with the heat load induced to the target by the SDDs and their electronics. Therefore, a quick calculation is performed [48]:

1. Each SDD array has an electrical power of ~ 40 mW. Taking into account that there are 48 arrays mounted around the target cell, the induced heating power thus can be supposed to be 2 W at maximum.
2. The electronic cabling of the SDDs also perform as a source of in flowing heat load. These are made of a combination of kapton and copper. Due to its low thermal conductivity, the kapton's contribution can be neglected. Using Equation 3.1 and the parameters of a single cable (L= 25 cm, A = 5 $\cdot 10^{-4}$ cm, ΔT = 200 K and $\lambda = 5$ Wcm^{-1}K^{-1} [50]) gives a maximum heat load of about 1 W for all cables combined.

As a result, it can be concluded, that the entire X-ray detection system introduces a maximum heat load of 3.0 W to the target cell.

Power	0.0 W	1.5 W	3.0 W
Diode 1 (K)	16.575 ± 0.003	18.488 ± 0.002	20.060 ± 0.002
Diode 2 (K)	15.758 ± 0.003	17.964 ± 0.002	19.752 ± 0.002
PT1 (K)	59.236 ± 0.009	76.164 ± 0.013	92.386 ± 0.016
PT2 (K)	63.834 ± 0.011	80.112 ± 0.013	95.355 ± 0.020
PT3 (K)	66.144 ± 0.009	78.699 ± 0.016	91.251 ± 0.016
PT5 (K)	75.440 ± 0.015	79.208 ± 0.017	82.776 ± 0.018

Table 16: Final temperatures reached during the first tests of the SIDDHARTA-2 target cell.

4.3.3 Measurements and Results

First Setup

In order to determine the temperatures reached on the Al plates surrounding the target, the entire structure is cooled down. The temperatures measured during the cooling process are presented in Figure 52 (a)-(b) for the two diodes on the aluminium rods and in (c)-(d) for the PT-1000s. The presented data are taken using the first target cell setup. Unfortunately, PT4 (located on the backside of plate 2) malfunctioned after about one hour, stopping the recording process. Therefore, Figure 52 (c) shows a gap where the malfunction remained undetected.

After the final temperatures are reached, the target cell is filled with helium of 4.6 purity to a pressure of around 0.5 bar. Then, two sets of measurements are performed. Firstly, the target cell is heated with an input power of 0.25 W on all six heating resistors, respectively. Therefore, the total input power is 1.5 W, a little below the heat load expected for the SDDs alone. Secondly, the input power is increased to 0.5 W for each resistor, making the total input power 3.0 W, representing the maximum heat load supposed for the X-ray detectors and their cabling. The resulting temperatures are measured using the software provided by Lake Shore and Pico Technology, respectively. Figure 53 presents the data taken by all temperature sensors during both heating stages. The final temperatures are extracted by calculating the mean and the standard deviation of the last 100 data points. This was done using Excel for the DT-670 diodes and using Python for the PT-1000 resistors. The results are listed in Table 16. These show a good temperature difference between the aluminium holder cooling the target cell, and the SDD plates for 0.0 W. With rising input power, the temperature rises for the plates as well as the Al holder. However, the final temperature values measured for the aluminium holder for cooling the target cell is still around 20 K which, as expected, is lower than the goal temperature for the target cell in the final experimental setup. The most important aspect of these results is the fact that the final temperatures reached by the plates during heating with 3.0 W remain still below 120 K. This indicates that the thermal contact between plates and target needs to be further reduced.

Since the PT-1000 positioning during this measurement clustered around Plates 1 and 2 and with PT5 being the only sensor not positioned on a plate with a heating resistor, a second arrangement was designed.

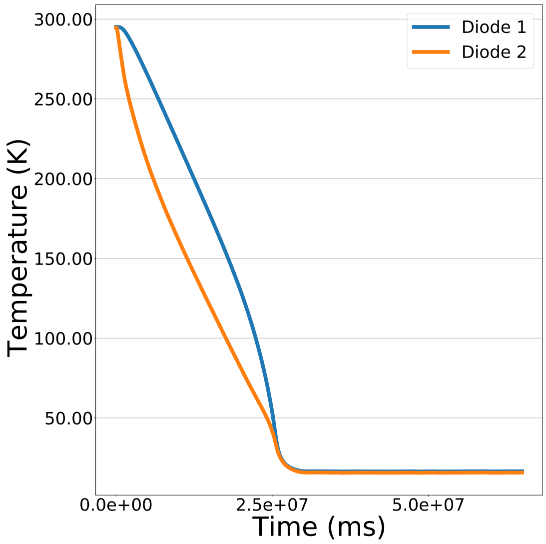

(a) Temperatures on the Al rods measured during the cooling process.

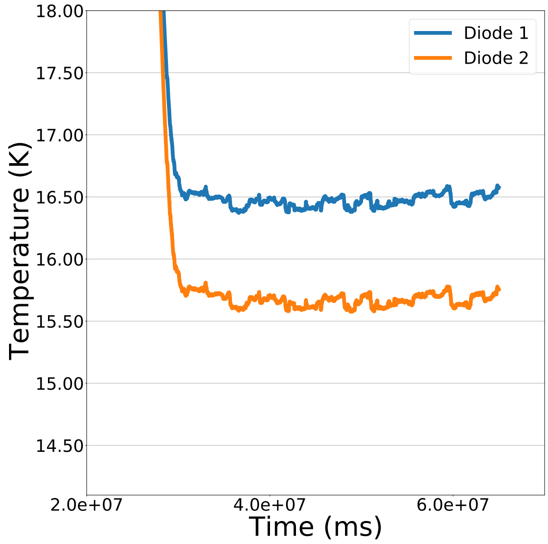

(b) Final temperatures reached on the Al rods. Diode 1 is located on the end closer to the cold head's sample holder. Diode 2 is mounted near the target cell.

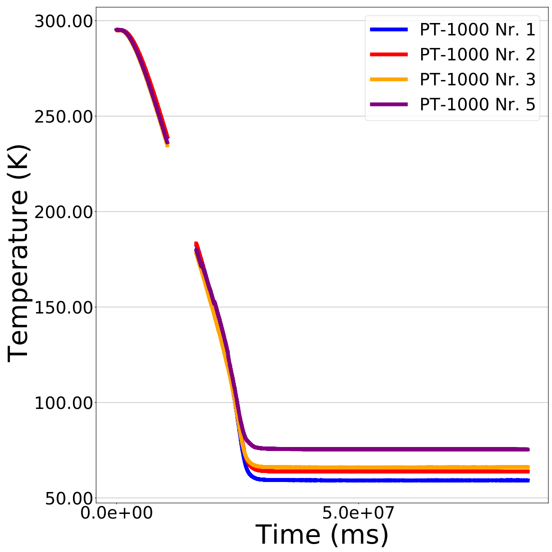

(c) Temperatures on the aluminium plates around the target cell measured during the cooling process.

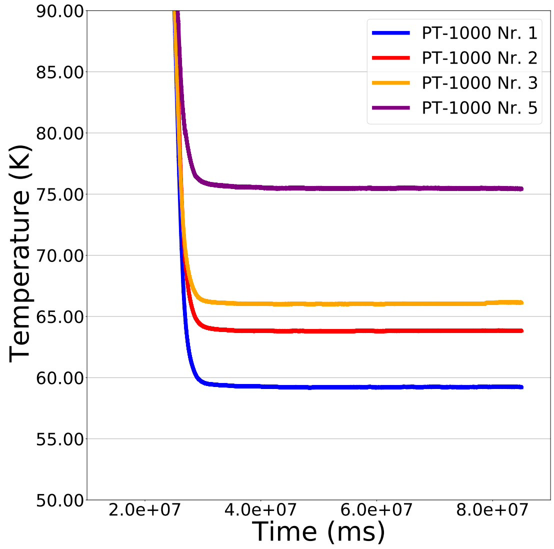

(d) Final temperatures reached on Al plates.

Figure 52: The cooling process measured on Al rods and plates around the target cell. The gap visible in (c) is a result of a malfunction of PT4.

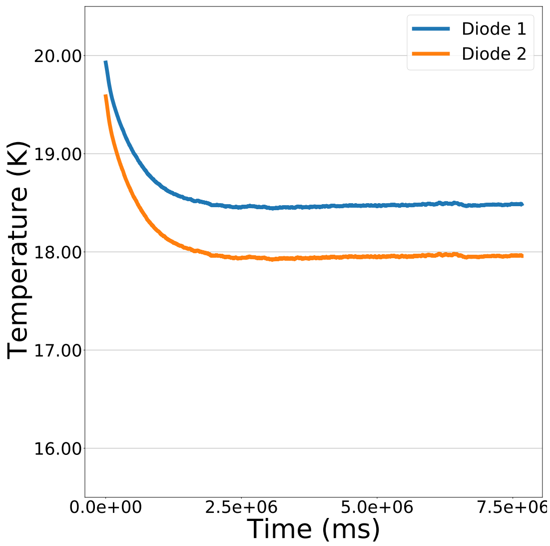

(a) Temperatures on the Al rods measured with 1.5 W heating power.

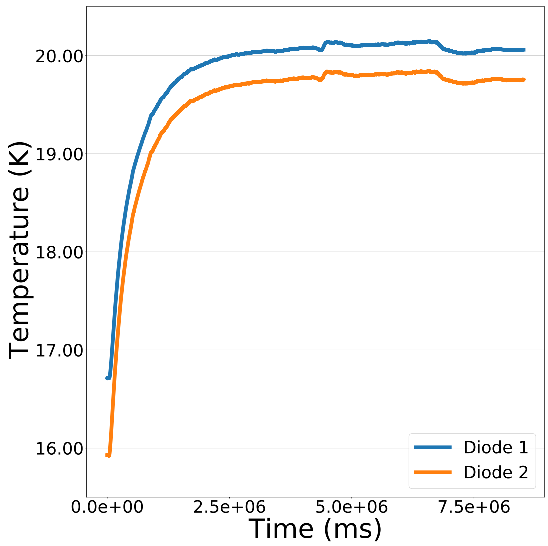

(b) Temperatures on the Al rods measured with 3.0 W heating power.

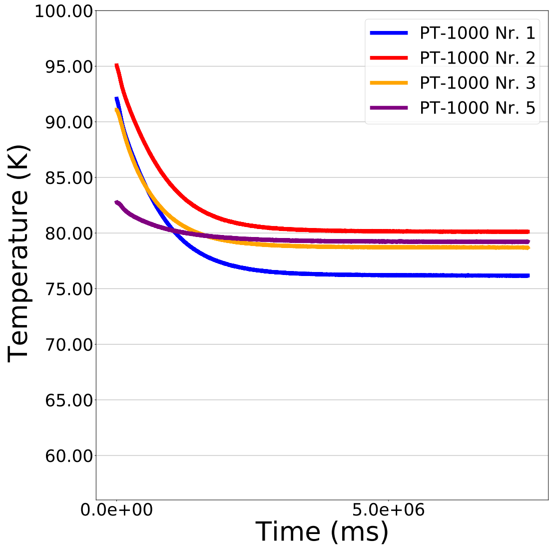

(c) Temperatures on the plates measured with 1.5 W heating power.

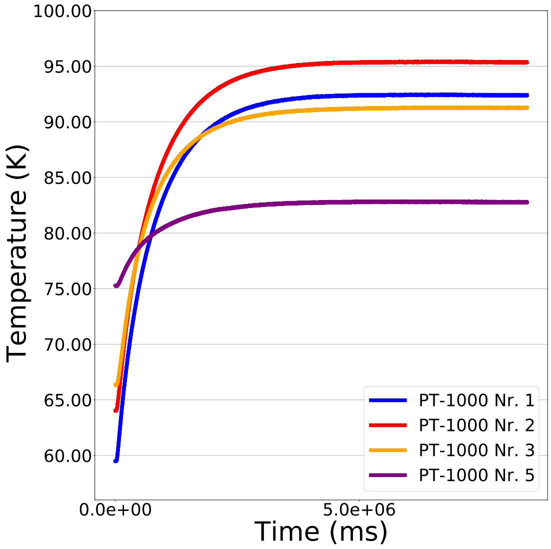

(d) Temperatures on the Al plates measured with 3.0 W heating power.

Figure 53: Data taken during the measurements performed with 1.5 W and 3 W heating power input.

Power	0.0 W	2.0 W	3.0 W
Diode 1 (K)	18.679 ± 0.005	21.800 ± 0.002	23.431 ± 0.003
Diode 2 (K)	16.323 ± 0.004	18.734 ± 0.002	19.958 ± 0.003
PT1 (K)	44.660 ± 0.006	54.388 ± 0.008	60.344 ± 0.009
PT2 (K)	59.543 ± 0.009	76.575 ± 0.014	86.486 ± 0.011
PT3 (K)	43.265 ± 0.006	53.115 ± 0.007	59.028 ± 0.008
PT4 (K)	48.713 ± 0.006	59.050 ± 0.008	65.052 ± 0.007
PT5 (K)	57.077 ± 0.009	70.648 ± 0.013	78.045 ± 0.013
PT6 (K)	46.236 ± 0.007	60.470 ± 0.009	68.701 ± 0.013

Table 17: Final temperatures reached during the second tests of the SIDDHARTA-2 target cell.

Second Setup

The new target cell arrangement used is shown in Figure 51. After cooling down, the target is again filled with around 0.5 bar of helium. Then, the structure is heated once with an input power of 0.3 W per resistor (2 W total) and once with 0.5 W per resistor (3 W total) in order to simulate the SDDs' and cables' influence on the temperature. Each of these measurements was performed over a period of about two hours until equilibrium was reached. The taken data for both power inputs is printed in Figure 54. The resulting temperatures are presented in Table 17. The values and uncertainties are determined as described above.

4.3.4 Conclusion and Outlook

Two configurations of new SDD holder arrangements have been tested for this thesis. When comparing the results from Tables 16 and 17, the differences between the two measurements become immediately obvious. First of all, the temperatures of the aluminium holder are higher in the second than in the first measurement. Secondly, the exact opposite is true for the aluminium plates. This indicates a better thermal contact between the holder and the target for the second measurement. This is an important indicator for the final experimental setup. As shown by the second measurement, the plates are cooled down considerable more due to a better contact between the Al holder and the target cell. Thus, it can be concluded that an improved thermal insulation between the target and the SDDs' plates is necessary for providing the desired temperature gradient. In addition, a layer of superinsulation could be added between the target's kapton foil and the aluminium plates. This is expected to bring the temperature of the X-ray detectors closer to 120 K.

Testing of such techniques will be done over the coming weeks at SMI. The final design will be installed into the SIDDHARTA-2 experiment at the DAΦNE collider facility in summer of 2021.

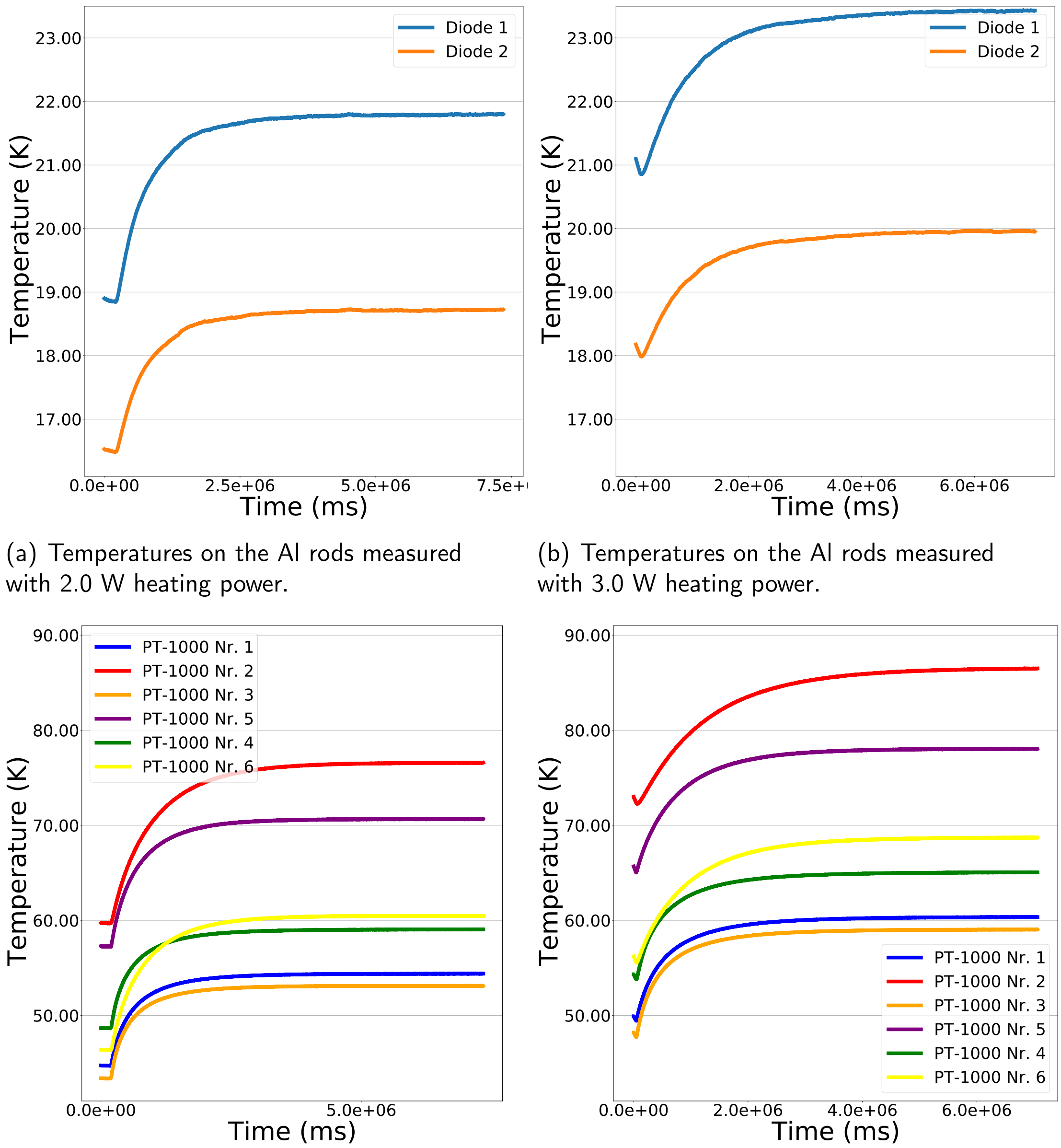

(a) Temperatures on the Al rods measured with 2.0 W heating power.

(b) Temperatures on the Al rods measured with 3.0 W heating power.

(c) Temperatures on the plates measured with 2.0 W heating power.

(d) Temperatures on the Al plates measured with 3.0 W heating power.

Figure 54: Data taken with the second target cell arrangement. The power input is 2.0 W and 3.0 W.

A Appendix: Temperatures for Rod and Strip Measurements

Power (W)	Temp. Diode 1 (K)	Temp. Diode 2 (K)	Temp. Diode 3 (K)	Temp. Diode 4 (K)
0.25	7.587 ± 0.005	7.440 ± 0.008	7.308 ± 0.007	7.231 ± 0.010
0.50	8.587 ± 0.008	8.450 ± 0.008	8.198 ± 0.008	7.906 ± 0.010
1.00	9.973 ± 0.006	9.812 ± 0.007	9.396 ± 0.007	8.869 ± 0.012
1.50	11.621 ± 0.006	11.448 ± 0.010	10.856 ± 0.019	10.119 ± 0.037
2.00	12.938 ± 0.027	12.836 ± 0.013	11.989 ± 0.010	11.090 ± 0.034

Table 18: First measurement of 5N aluminium rods with power supplied by Resistors 1 and 2.

Power (W)	Temp. Diode 1 (K)	Temp. Diode 2 (K)	Temp. Diode 3 (K)	Temp. Diode 4 (K)
0.25	7.690 ± 0.007	7.512 ± 0.005	7.389 ± 0.008	7.288 ± 0.010
0.50	8.782 ± 0.007	8.617 ± 0.007	8.360 ± 0.007	8.028 ± 0.010
1.00	10.272 ± 0.007	10.098 ± 0.005	9.657 ± 0.008	9.075 ± 0.022
1.50	11.911 ± 0.007	11.757 ± 0.013	11.110 ± 0.013	10.299 ± 0.021
2.00	13.097 ± 0.014	12.958 ± 0.018	12.106 ± 0.025	11.242 ± 0.020

Table 19: Second measurement of 5N aluminium rods with power supplied by Resistors 1 and 2.

Power (W)	Temp. Diode 1 (K)	Temp. Diode 2 (K)	Temp. Diode 3 (K)	Temp. Diode 4 (K)
0.50	10.338 ± 0.012	10.381 ± 0.013	9.986 ± 0.014	9.521 ± 0.004
1.00	10.580 ± 0.009	10.476 ± 0.005	9.983 ± 0.009	9.400 ± 0.030
0.50	10.342 ± 0.012	10.370 ± 0.004	9.976 ± 0.011	9.539 ± 0.042
1.00	10.598 ± 0.013	10.492 ± 0.018	10.018 ± 0.013	9.457 ± 0.013

Table 20: Stabilised measurements of the aluminium rods. Upper two rows represent the first, lower two rows the second measurement. Resistor 3 regulates Diode 3 to 10 K, the given input power is supplied by Resistors 1 and 2.

Power (W)	Temp. Diode 1 (K)	Temp. Diode 2 (K)	Temp. Diode 3 (K)	Temp. Diode 4 (K)
1.0	7.108 ± 0.018	7.086 ± 0.016	5.823 ± 0.024	5.797 ± 0.009
2.0	8.008 ± 0.016	8.021 ± 0.020	6.280 ± 0.013	6.281 ± 0.011
3.0	9.402 ± 0.007	9.393 ± 0.020	7.29 ± 0.12	7.172 ± 0.067
4.0	10.625 ± 0.030	10.610 ± 0.003	8.16 ± 0.22	8.04 ± 0.23

Table 21: Temperatures taken during the first single Al strip measurement.

Power (W)	Temp. Diode 1 (K)	Temp. Diode 2 (K)	Temp. Diode 3 (K)	Temp. Diode 4 (K)
1.0	7.051 ± 0.021	7.024 ± 0.026	5.791 ± 0.013	5.774 ± 0.022
2.0	7.952 ± 0.017	7.895 ± 0.019	6.243 ± 0.023	6.204 ± 0.022
3.0	9.273 ± 0.046	9.236 ± 0.046	7.30 ± 0.15	7.28 ± 0.13
4.0	10.489 ± 0.040	10.480 ± 0.044	8.13 ± 0.18	8.14 ± 0.16

Table 22: Temperatures taken during the second single strip measurement.

Power (W)	Temp. Diode 1 (K)	Temp. Diode 2 (K)	Temp. Diode 3 (K)	Temp. Diode 4 (K)
1.0	6.480 ± 0.022	6.505 ± 0.022	5.807 ± 0.019	5.800 ± 0.025
2.0	7.288 ± 0.023	7.328 ± 0.035	6.326 ± 0.016	6.345 ± 0.020
3.0	8.483 ± 0.043	8.452 ± 0.040	7.258 ± 0.037	7.218 ± 0.047
4.0	9.528 ± 0.014	9.544 ± 0.032	8.22 ± 0.13	8.12 ± 0.11

Table 23: Temperatures taken during the first double Al strip measurement.

Power (W)	Temp. Diode 1 (K)	Temp. Diode 2 (K)	Temp. Diode 3 (K)	Temp. Diode 4 (K)
1.0	6.497 ± 0.087	6.460 ± 0.050	5.94 ± 0.10	5.88 ± 0.13
2.0	7.252 ± 0.010	7.269 ± 0.023	6.379 ± 0.087	6.320 ± 0.011
3.0	8.437 ± 0.044	8.504 ± 0.053	7.255 ± 0.035	7.318 ± 0.058
4.0	9.345 ± 0.074	9.43 ± 0.11	8.14 ± 0.23	8.270 ± 0.092

Table 24: Temperatures taken during the second double aluminium strip measurement.

Power (W)	Temp. Diode 1 (K)	Temp. Diode 2 (K)	Temp. Diode 3 (K)	Temp. Diode 4 (K)
1.0	7.676 ± 0.034	7.744 ± 0.015	6.228 ± 0.005	6.215 ± 0.075
2.0	8.818 ± 0.004	8.854 ± 0.016	6.728 ± 0.071	6.780 ± 0.084
3.0	10.480 ± 0.020	10.497 ± 0.028	7.830 ± 0.081	7.829 ± 0.034
4.0	12.309 ± 0.010	12.322 ± 0.020	8.81 ± 0.12	8.865 ± 0.074

Table 25: Temperatures taken during the first measurement using indium as conducting agent between the Al strips and the holders.

Power (W)	Temp. Diode 1 (K)	Temp. Diode 2 (K)	Temp. Diode 3 (K)	Temp. Diode 4 (K)
1.0	7.663 ± 0.015	7.697 ± 0.015	6.067 ± 0.019	6.052 ± 0.016
2.0	8.858 ± 0.005	8.896 ± 0.012	6.738 ± 0.070	6.708 ± 0.074
3.0	10.499 ± 0.003	10.528 ± 0.015	7.728 ± 0.097	7.78 ± 0.11
4.0	12.261 ± 0.011	12.286 ± 0.008	8.74 ± 0.20	8.63 ± 0.17

Table 26: Temperatures taken during the first measurement using indium.

Power (W)	Temp. Diode 1 (K)	Temp. Diode 2 (K)	Temp. Diode 3 (K)	Temp. Diode 4 (K)
1.0	7.776 ± 0.015	7.845 ± 0.017	6.083 ± 0.022	6.050 ± 0.014
2.0	9.001 ± 0.015	9.045 ± 0.005	6.80 ± 0.14	6.690 ± 0.085
3.0	10.650 ± 0.013	10.700 ± 0.011	7.612 ± 0.028	7.632 ± 0.041
4.0	12.549 ± 0.013	12.566 ± 0.016	8.572 ± 0.061	8.519 ± 0.037

Table 27: Temperatures taken during the first measurement set of the bent foils.

Power (W)	Temp. Diode 1 (K)	Temp. Diode 2 (K)	Temp. Diode 3 (K)	Temp. Diode 4 (K)
1.0	7.793 ± 0.020	7.825 ± 0.036	6.292 ± 0.071	6.214 ± 0.025
2.0	8.953 ± 0.013	8.995 ± 0.005	6.671 ± 0.011	6.698 ± 0.093
3.0	10.739 ± 0.007	10.763 ± 0.022	7.90 ± 0.12	7.938 ± 0.083
4.0	12.443 ± 0.013	12.457 ± 0.022	8.85 ± 0.12	8.883 ± 0.050

Table 28: Temperatures taken during the second measurement set of the bent foils.

Power (W)	Temp. Diode 1 (K)	Temp. Diode 2 (K)	Temp. Diode 3 (K)	Temp. Diode 4 (K)
1.0	7.833 $\pm$ 0.017	7.883 $\pm$ 0.019	6.166 $\pm$ 0.026	6.230 $\pm$ 0.044
2.0	8.927 $\pm$ 0.013	8.984 $\pm$ 0.013	6.665 $\pm$ 0.004	6.627 $\pm$ 0.024
3.0	10.599 $\pm$ 0.015	10.649 $\pm$ 0.016	7.636 $\pm$ 0.028	7.603 $\pm$ 0.028
4.0	12.419 $\pm$ 0.018	12.440 $\pm$ 0.002	8.84 $\pm$ 0.15	8.71 $\pm$ 0.21

Table 29: Temperatures taken during the third measurement set of the bent foils.

List of Figures

List of Tables

Acronyms

AD Antiproton Decelerator.

AMT ASACUSA Micromegas Tracker.

ASACUSA Atomic Spectroscopy And Collisions Using Slow Antiprotons.

BGO Bismuth Germanate.

C Charge.

CCD Charge-Coupled device.

CDC Cylindrical Drift Chamber.

CDH Cylindrical Detector Hodoscope.

CDS Cylindrical Detector System.

CERN Conseil Européen pour la Recherche Nucléaire.

DAΦNE Double Annular Φ Factory for Nice Experiments.

DEAR DAΦNE Exotic Atoms Research.

ELENA Extra Low Energy Antiproton.

G-M Gifford-McMahon.

GS-HFS Ground State Hyperfine Splitting.

HFS High Field Seekers.

IVC Inner Vacuum Chamber.

J-PARC Japan Proton Accelerator Research Complex.

KEK High Energy Accelerator Research Organization.

LFS Low Field Seekers.

LHC Large Hadron Collider.

LINAC LINear ACcelerator.

LNF National Laboratory of Frascati.

LS Long Shutdown.

Micromegas Micro-MEsh Gaseous Structure.

MRE Multi-Ring Electrode.

MRT Multi-Ring Trap.

MUSASHI Monoenergetic Ultra-Slow Antiproton Source for High-precision Investigation.

OFC Oxygen Free Copper.

OFHC Oxygen-Free High thermal Conductivity.

OVC Outer Vacuum Chamber.

P Parity.

PM Photo Multiplier.

PS Proton Synchrotron.

PSB Proton Synchrotron Booster.

QCD Quantum ChromoDynamics.

SDD Silicon Drift Detector.

SIDDHARTA Silicon Drift Detectors for Hadronic Atom Research by Timing Application.

SiPM Silicon PhotoMultiplier.

SM Standard Model.

SME Standard Model Extension.

SMI Stefan Meyer Institute for Subatomic Physics.

SPS Super-Proton Synchrotron.

T Time.

TMP TurboMolecular Pump.

References

[1] Inc. Brooks Automation. *Cryotiger. Cooling System*, 2005.

[2] G. Ventura and L. Risegari. *The Art of Cryogenics*. Elsevier, Oxford, UK, 2008.

[3] A.T.A.M. Waele. Basic Operation of Cryocoolers and Related Thermal Machines. *J Low Temp Phys*, 164:179–236, 2011.

[4] A.T.A.M. Waele. Basics of Joule-Thomson Liquefaction and JT Cooling. *J Low Temp Phys*, 186:385–403, 2017.

[5] SHI-APD Cryogenics Inc. *RDK-408D2 Cold Head*, 2005.

[6] SRDK-408D2 Cold Head Capacity Map (50 Hz). `http://www.shicryogenics.com/wp-content/uploads/2019/08/RDK-408D2_Capacity_Map.pdf`. Accessed: 31.10.2020.

[7] P. A. M. Dirac. The Quantum Theory of the Electron. *Proceeding of the Royal Society of London, Series A*, 117:610–624, 1928.

[8] C. D. Anderson. The Positive Electron. *Physical Review*, 43:491–494, 1933.

[9] O. Chamberlain et. al. Observation of Antiprotons. *Physical Review*, 100:947–950, 1955.

[10] D. Colladay and V. A. Kostelecky. Lorentz-Violating Extension of the Standard Model. *Physical Review D*, 58, 1998.

[11] V. A. Kostelecky R. Bluhm and N. Russell. CPT and Lorentz Tests in Hydrogen and Antihydrogen. *Physical Review Letters*, 82:2254–2257, 1999.

[12] E. Widmann et. al. Hyperfine spectroscopy of hydrogen and antihydrogen in ASACUSA. *Hyperfine Interact*, 240, 2019.

[13] A.Bianconi et. al. Measurement of the antiproton–nucleus annihilation cross section at 5.3 MeV. *Physics Letters B*, 704:461–466, 2011.

[14] Bernadette Kolbinger. *Machine Learning for Antihydrogen Detection in ASACUSA*. dissertation, University of Vienna, 2019.

[15] M. Hori et. al. Two-photon laser spectroscopy of antiprotonic helium and the antiproton-to-electron mass ratio. *Nature*, 475:484–488, 2011.

[16] I. I. Rabi et. al. A New Method of Measuring Nuclear Magnetic Moment. *Physical Review*, 53:318, 1938.

[17] I. I. Rabi et. al. The Molecular Beam Resonance Method for Measuring Nuclear Magnetic Moments The Magnetic Moments of ${}_3Li^6$, ${}_3Li^7$ and ${}_9F^{19}$. *Physical Review*, 55:526–535, 1939.

[18] Wolfgang Demtröder. *Experimentalphysik 3: Atome, Moleküle und Festkörper*. Springer-Verlag, Berlin Heidelberg, 2009.

[19] Y. Nagata et. al. Progress of Antihydrogen Beam Production Using a Double CUSP Trap. In *: 12th International Conference on Low Energy Antiproton Physics (LEAP 2016)*, 2017.

[20] Antiproton decelerator cern. https://upload.wikimedia.org/wikipedia/commons/c/c8/Antiproton_Decelerator_CERN.svg. Accessed: 30.11.2020.

[21] M. Shamsuzzoha Basunia. ^{22}Na. https://www.nndc.bnl.gov/nudat2/decaysearchdirect.jsp?nuc=22NA&unc=nds, Accessed: 30.11.2020. Nuclear Data Sheet 127, 69 (2015).

[22] H Imao et. al. Positron Accumulation and Manipulation for Antihydrogen Synthesis". *Journal of Physics: Conference Series*, 225:012018, 2010.

[23] Cern's accelerator complex. https://home.cern/science/accelerators/accelerator-complex, Accessed: 1.12.2020.

[24] J. Walz M. Hori. Physics at CERN's Antiproton Decelerator. *Progress in Particle and Nuclear Physics*, 72:206–253, 2013.

[25] N. Kuroda et. al. Confinement of a Large Number of Antiprotons and Production of an Ultraslow Antiproton Beam. *Physical Review Letters*, 94:023401, 2005.

[26] Silke Federmann. *A Spin-Flip Cavity for Microwave Spectroscopy of Antihydrogen*. dissertation, University of Vienna, 2012.

[27] M. Diermaier et. al. An Atomic Hydrogen Beam to Test ASACUSA's Apparatus for Antihydrogen Spectroscopy. *Hyperfine Interact*, 233:35–40, 2015.

[28] M. Shibata et. al. Compact Cryogenic system with Mechanical Cryocoolers for Antihydrogen Synthesis. *Review of Scientific Instruments*, 79:015112, 2007.

[29] RDE-418D4 4K Ccyocooler Series Data Sheet. http://www.shicryogenics.com/wp-content/uploads/2019/05/RDE-418D4-Datasheet.pdf, Accessed: 3.02.2021.

[30] A. L. Woodcraft. Recommended Values for the Thermal Conductivity of Aluminium of Different Purities in the Cryogenic to Room Temperature Range, and a Comparison with Copper. *Cryogenics*, 45:626–636, 2005.

[31] Prophysik AG. *Datenblatt Membranbalg DN 63CF*.

[32] E. Fermi and E. Teller. The Capture of Negative Mesotrons in Matter. *Physical Review*, 72:399–408, 1947.

[33] P.A. Zyla et al. (Particle Data Group). 2020 Review of Particle Physics. *Prog. Theor. Exp. Phys.*, 083C01, 2020.

[34] D. Gotta. Precision spectroscopy of Light Exotic Atoms. *Progress in Particle and Nuclear Physics*, 52:133–195, 2004.

[35] S. Deser et. al. Energy Level Displacements in Pi-Mesonic Atoms. *Physical Review*, 93:774–776, 1954.

[36] T.L.Trueman. Energy Level Shifts in Atomic States of Strongly-Interacting particles. *Nuclear Physics*, 26, 1961.

[37] W. Weise W. Horiuchi, H. Hyodo. Kaonic Deuterium and Low-Energy Antikaon-Nucleon Interaction. *EPJ Web of Conferences*, 164, 2018.

[38] A. Rusetsky U.-G. Meißner, U. Raha. Spectrum and Decays of Kaonic Hydrogen. *The European Physical Journal C*, 35:349–357, 2004.

[39] C. Curceanu et. al. The Modern Era of Light Kaonic Atom Experiments. *Reviews of Modern Physics*, 91:025006, 2019.

[40] M. Iwasaki et. al. Observation of Kaonic Hydrogen K_α X-Rays. *Physical Review Letters*, 78:3067–3069, 1997.

[41] G. Beer et. al.(Dear collaboration). Measurement of the Kaonic Hydrogen X-Ray Spectrum. *Physical Review Letters*, 94:212302, 2005.

[42] M. Bazzi et. al.(SIDDHARTA collaboration). A New Measurement of Kaonic Hydrogen X-rays. *Physics Letters B*, 704:113–117, 2011.

[43] M. Faber et. al. Energy Level Displacement of Excited np State of Kaonic Deuterium in Faddeev Equation Approach. *Physical Review C*, 84, 2011.

[44] M. Tüchler et. al. A Charged Particle Veto Detector for Kaonic Deuterium Measurements at DAΦNE. *Journal of Physics: Conference Series*, 1138, 2018.

[45] K. Agari et. al. The K1.8BR spectrometer system at J-PARC. *Progress of Theoretical and Experimental Physics*, 2012, 2012.

[46] J. Zmeskal. From Kaonic Atoms to Kaonic Nuclei: A Search for Antikaon-Mediated Bound Nuclear Systems. *Progress in Particle and Nuclear Physics*, 61:512–550, 2008.

[47] Dafne. `http://w3.lnf.infn.it/accelerators/dafne/?lang=en`, Accessed: 22.01.2021.

[48] J. Zmeskal. Private communication.

[49] Uli Köhler. Utilities regarding RTDs. `https://github.com/ulikoehler/UliEngineering/blob/master/UliEngineering/Physics/RTD.py`, Accessed: 2.12.2020.

[50] Properties of Selected Materials at Cryogenic Temperatures. `https://tsapps.nist.gov/publication/get_pdf.cfm?pub_id=913059`, Accessed: 11.03.2021.